2015-07-20

Infrared Spectroscopy of CS2 and C2D2 Binary and Ternary complexes

Yousefi Koopaei, Mahdi

UNIVERSITY OF CALGARY

Infrared Spectroscopy of CS_2 and C_2D_2 Binary and Ternary complexes

by

Mahdi Yousefi Koopaei

A THESIS

SUBMITTED TO THE FACULTY OF GRADUATE STUDIES

IN PARTIAL FULFILMENT OF THE REQUIREMENTS FOR THE

DEGREE OF MASTER OF SCIENCE

GRADUATE PROGRAM IN PHYSICS AND ASTRONOMY

CALGARY, ALBERTA

JULY, 2015

Abstract

Density Functional Theory (DFT) calculations using CAM-B3LYP hybrid functional were performed on the binary and ternary van der Waals complexes formed from CS_2 and C_2D_2 monomers. Theoretical stationary structures were found. The geometrical parameters of stationary structures were optimized and their theoretical rotational constants were obtained. The calculations predict a planar parallel configuration with C_{2v} symmetry as the lowest energy isomer of CS_2-C_2D_2 dimer. These calculations also show that a T-shaped structure with C_{2v} symmetry is the higher energy isomer. They also indicate that a twisted-barrel configuration with C_2 symmetry is the minimum energy isomer of $(CS_2)_2$-C_2D_2 mixed trimer. In addition, the two minimum energy isomers of CS_2-$(C_2D_2)_2$ trimer were found. The global minimum structure has a distorted T-shaped C_2D_2 dimer unit with a CS_2 monomer "above" the dimer and the higher energy isomer has a planar configuration.

In agreement with the DFT calculations, rotationally-resolved infrared spectra of the parallel isomer of CS_2-C_2D_2 and the twisted barrel shaped isomer of $(CS_2)_2$-C_2D_2 trimer were observed and simulated in the region of C_2D_2 ν_3 (~2439 cm^{-1}) stretching fundamental. The complexes were generated in a supersonic slit-jet apparatus and probed using an Optical Parametric Oscillator (OPO). The observed band of CS_2-C_2D_2 dimer is centered at 2438.16 cm^{-1} whereas the band for the $(CS_2)_2$-C_2D_2 trimer is centered at 2436.73 cm^{-1}. Both bands indicate red shifts with respect to C_2D_2 ν_3 fundamental band origin (2439.244 cm^{-1}). The observed rotational constants are in good agreement with those obtained from the DFT calculations

Acknowledgements

I wish to express my gratitude to all who made this thesis possible. I owe the deepest gratitude to Dr. Nasser Moazzen-Ahmadi for his support, tolerance, encouragement and persistent help over the years. Without his guidance this thesis would not have been possible. I appreciate the supervisory committee members Dr. Ann-Lise Norman, Dr. Arvi Rauk and Dr. Michael Wieser for agreeing to review this thesis.

I am also very grateful to Dr.Jalal Norooz-Oliaee and Dr. Mojtaba Razaei for scientific support and training. I am courteous to my supervisor and physics department for financial support. I thank Sahar Sheybani-Deloui for her comments and feedbacks on the thesis. Also, thanks to my colleagues Jobin George, Luis Welbanks and Aaron Barclay for their help in the lab and interesting discussions.

Table of Contents

List of Tables

List of Figures and Illustrations

List of Symbols, Abbreviations and Nomenclature

DFT	Density Functional Theory
vdW	van der Waals
C_2D_2	Deuterated Acetylene
CS_2	Carbon Disulfide
Dimer	Two monomer complex
Trimer	Three monomer complex
OPO	Optical Parametric Oscillator
PES	Potential Energy Surface
IR	Infrared
QCL	Quantum Cascade Laser
CO_2	Carbon Dioxide
N_2O	Nitrous Oxide
OCS	Carbonyl sulfide
MP2	Second order Moller-Plesset
SCF	Self-Consistent Field
HF	Hartree-Fock
LDA	Local Density Approximation
GGA	Generalized Gradient Approximation
B3LYP	Becke 3-term Lee,Yang, and Parr
G09	Gaussian 09
FEM	Finite Element Method

AO	Atomic Orbital
STO	Slater Type Orbital
GTO	Gaussian Type Orbital
A, B, C	Rotational constants of the molecule
RMS	Root Mean Square
SRO	Singly Resonant Optical parametric oscillator
PPLN	Periodically Poled Lithium Niobate
MgO	Magnesium Oxide
MOPA	Master Oscillator Power-Amplifier
cw	Continues Wave
PZT	Lead Zirconate Titantate
DC	Direct Current
CaF_2	Calcium Fluoride
SNR	Signal to Noise Ratio
TTL	Transistor-Transistor Logic
DAQ	Data Acquisition card
FIR	Finite Impulse Response
PMIFST	Principal Moment of Inertia From Structure

Chapter One: Introduction

1.1 Van der Waals interaction

Molecules, from gaseous to condensed states, are held together by competition of attractive and repulsive forces. These forces play a significant role in a wide range of physical and chemical process such as condensation, solvation, phase transition, melting and boiling points, viscosity and specific heat capacity. A simple example that shows the role of intermolecular interactions is water molecules in a glass [1]. In the absence of attractive forces, the water molecules would spread around. Moreover, because the intermolecular forces are highly repulsive at small ranges, water cannot be compressed to a smaller volume with ease. The attractive intermolecular forces are categorized into four types 1) van der Waals, 2) hydrogen bonding, 3) hydrophobic interaction and 4) ionic interaction; among which van der Waals forces are the weakest [2]. This was first noticed by Johannes Diderik Van der Wals in 1873. He concluded that the non-zero size of molecules and the intermolecular forces should be considered in the ideal gas law as [3]:

$$(P + a/V^2)(V - b) = Nk_BT \tag{1.1}$$

In equation (1.1), the constant b stands for the volume occupied by the molecules. Thus, volume in the ideal gas law is replaced by $(V - b)$. Due to the attractive forces, the molecules exert less pressure to the walls of the container which is modeled by $P+ a/V^2$. Here a is a constant that represents the attraction between the molecules [4].

Van der Waals forces may arise from three sources [5]: force between two permanent dipoles (Keesom force), force between a permanent dipole and a corresponding induced dipole (Debye force) and force between two instantaneously induced dipoles (London dispersion force). The

potential for the interaction of dipoles brought together from infinite separation to a finite distance r, when their angular distribution is taken into account is proportional to the inverse-sixth power of the distance.

On the other hand, at short intermolecular separations, repulsive electrostatic forces become important. Repulsive forces are caused by electrostatic forces between negatively charged electron clouds and also between the positively charged nuclei of nearby molecules. Electrostatic repulsion is the dominant force in the short ranges whereas the dominant force in the long-ranges is the attractive Van der Waals force. Taken together, the attractive Van der Waals force and the repulsive electrostatic force result in a potential curve with a shallow minimum resembling a Morse potential or a Lennard-Jones potential along a given coordinate as shown in Figure 1-1.

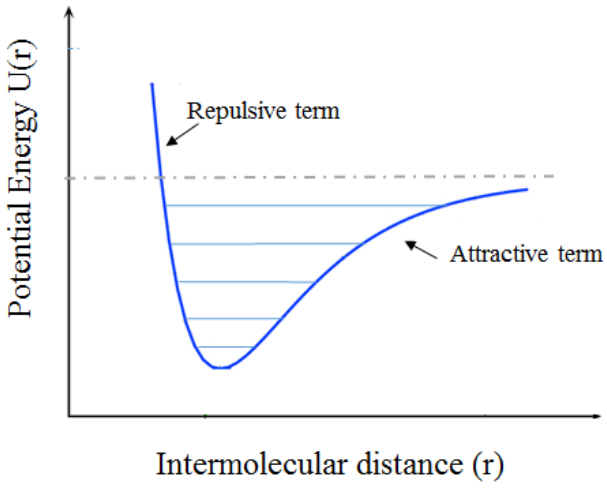

Figure 1-1: The potential energy curve due to the sum of repulsive and attractive contributions.

Molecular complexes are defined as two or more monomers which are held together in a potential minimum. Individual molecules attract each other to form larger size clusters which are a bridge between the gas and condensed phases. Because of small binding energies and thermal agitations, van der Waals bonds are easily broken at room temperature. One must therefore study

van der Waals clusters in a collision free environment and at very low rotational temperatures. Supersonic jet expansion of a buffer gas such as He, Ne or Ar seeded by desired monomers whose molecular clusters are to be studied provide such environments.

Information found by investigation of van der Waals forces is key to understanding many interesting molecular phenomena in nature such as aerosol formation [6], protein configuration [7], the structure of DNA complexes [8], adsorption of atoms and molecules on surfaces [9] energy transfer, line broadening and cluster formation. The research on van der Waals forces would be helpful in understanding the intermolecular interactions between molecules in bulk matter; which are responsible for properties of condensed phases and collisional dynamics. Exploration of these forces would help in constructing accurate potential energy surface (PES). Furthermore, by the investigation of larger clusters information on many-body interactions and non-additive effects can be extracted.

1.2 Methodology of study

The theoretical understanding of molecular structures can be very valuable in predicting molecular properties, characterizing condensation pathways, constructing accurate PES, and etc. There is a range of techniques used for theoretical investigation of van der Waals complexes, and arguably one of the most reliable methods is the density functional theory (DFT) methods. DFT is presently one of the most successful theoretical approach to compute the ground state properties of a system in a vast class of materials, ranging from atoms and molecules to sophisticated complexes. DFT calculation has been used to predict a great variety of molecular properties such as molecular structures, vibrational frequencies, binding energies, electric and magnetic properties and etc. With the availability of high power computers and their parallel processing capabilities, it

is possible to use DFT methods for calculations of complicated systems with relative ease. Gaussian 09 software, used in this study, is a package for computational chemistry, which employs the DFT methods to predict the stationary structures of molecular clusters.

On the other hand, experimental observations remain essential in providing researchers with the most direct measurements of intermolecular forces. Experimental observations can be carried out using high resolution spectroscopy. High resolution infrared (IR) spectroscopy employed in our lab, provides structural information, vibrational shifts, and vibrational frequency for intermolecular modes, all of which can be used as bench mark for *ab initio* calculations. Weakly-bound molecular clusters are generated in a supersonic jet. They are formed by adiabatic expansion of the desired gas molecules, seeded in a carrier gas, from a gas chamber at high pressure into a low pressure region through circular or slit-shaped nozzles. The formed clusters are then probed by tunable lasers such as lead-salt diode laser, Quantum Cascade Laser (QCL) or Optical Parametric Oscillator (OPO) operating in the rapid-scan signal averaging mode. The obtained absorption spectra which consist of ro-vibrationally resolved lines are recorded by detection of the laser intensity using a LabVIEW based data acquisition package. Finally, the recorded spectra are analyzed and simulated with the aid of the PGOPHER program.

1.3 Spectroscopy of "CO_2 family" with acetylene

Dimers and larger clusters formed from the "CO_2 family" of monomers, CO_2, N_2O and OCS, with acetylene have been extensively studied by high resolution infrared spectroscopy [10-31]. However, weakly-bound molecular complexes of CS_2, another member of this family, have not been studied. The present study is concerned with the spectroscopic identification and observation of complexes formed from CS_2 and deuterated acetylene. Deuterated acetylene was used as the

chromophore, because it has a strong band in the frequency range of the OPO probe. The main question in this study is what would be the stable structures of these complexes and whether they have similar structures to other members of the "CO_2 family". In the following sections an overview of previous studies on similar complexes in the context of the present work is given followed by outline of the thesis.

1.3.1 Observation of CO_2–C_2H_2 Dimer

The first experimental observation of CO_2–C_2H_2 complex was made in 1988 by Prichard et al [11]. The spectra were recorded by excitation of the C-H asymmetric stretching fundamental. Their results indicated that the observed CO_2–C_2H_2 structure has C_{2v} symmetry in which the monomers were found to be parallel and the line joining their centres of masses is perpendicular to the monomers axes. One year later, near infrared laser molecular beam spectroscopy of this complex was reported by Huang, and Miller [12]. Their results, at higher resolution, were in a good agreement with those reported by Prichard et al [11]. In the same year, Muenter reported the observation of the microwave spectrum of this dimer [13] where the rotational constants and centrifugal distortion were measured for both CO_2–C_2H_2 and CO_2–C_2D_2. CO_2 and C_2H_2 monomers have no dipole moment. However, the complex has a rotational spectrum because of induced dipole moment along the monomers. The quadrupole moment of each molecule generates a polarizing field at the other molecule. The generated fields induce a dipole in the complex.

In 2011, the fundamental and a torsional combination band of CO_2–C_2H_2 dimer were observed in the region of CO_2 ν_3 fundamental band (~2349 cm^{-1}) by Lauzin et al [14]. They found a torsional frequency of 44.385 cm^{-1} which is in good agreement with Muenter's prediction of 40 cm^{-1} [13] based on the microwave data. This cluster has also been studied in the C–H stretching overtone

region [15-16]. Recently, a study of a fundamental and several combination bands of CO_2–C_2H_2 and CO_2–C_2D_2 in the mid infrared region was reported [17]. Five bands were analyzed in which four were assigned as combination bands. These included the fundamental asymmetric stretch of the C_2D_2 subunit, two combination bands involving the out-of-plane torsional vibrations for CO_2–C_2D_2, and two combination bands involving an intermolecular in-plane bending vibration for CO_2–C_2H_2 and CO_2–C_2D_2.

In 1990, an *ab initio* calculation was performed using second order Moller-Plesset perturbation theory (MP2) by Bone and Handy [18]. In addition to the global minimum energy isomer with C_{2v} symmetry, they found a higher energy co-linear form of CO_2–C_2H_2. These lowest energy isomers are shown in Figure 1-2. In the same year, Almeida at al. published an *ab initio* study of CO_2–C_2H_2 using Self-Consistent Field (SCF) level of theory. They reported the same minimum energy structures, parallel and linear, in addition to harmonic vibrational frequencies. Moreover, they showed that the T-shape configurations are not stationary points on the PES [19].

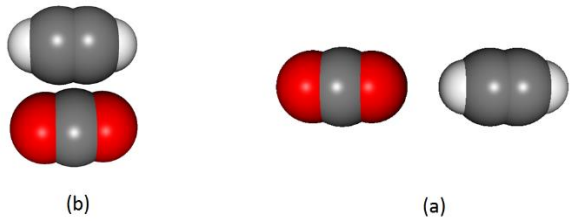

Figure 1-2: Stationary configuration of CO_2-C_2H_2 with dimer: a) global minimum with parallel structure and C_{2v} symmetry; b) local minimum with linear configuration.

1.3.2 Observation of OCS–C_2H_2 Dimer

Using microwave spectroscopy, Peebles and Kuczkowski [20, 21] came to the conclusion that there are two planar isomers of OCS–C_2H_2 as depicted in Figure 1-3. The most stable isomer has a slipped near-parallel configuration with C_s symmetry. The second isomer was observed to be a

T-shaped with C_{2v} symmetry in which OCS monomer forms the stem of the T and the S-atom interacting with the C_2H_2 triple bond. Using semi-empirical and *ab initio* calculations, they concluded that the near-parallel isomer is the minimum energy form [21]. Recently, the first infrared observation of OCS–C_2H_2 and OCS–C_2D_2 was reported by Norooz Oliaee et al. in the OCS ν_1 region [22]. They reported rotational parameters for the excited vibrational state and vibrational shifts. When argon was used as the carrier gas, the T-shaped isomer disappeared. This observation is in agreement with the theoretical calculations [21] showing that the near-parallel isomer is the minimum energy form.

Figure 1-3: Stationary structure of OCS-C_2H_2 dimer: a) lowest energy isomer which is near parallel structure; b) next higher order energy isomer with T-shape structure [22].

1.3.3 Observation of the ternary mixed complexes of OCS and C_2H_2

One purpose of investigation of trimers is to probe the effects of adding a third body to the two-body interaction such as non-additive effects. This as well initiates the study of the many-body interactions. The first observation of mixed trimers containing a "CO_2 family" member and acetylene, was the high-resolution spectroscopy of complexes containing C_2H_2 and OCS. Peebles and Kuczkowski observed $(OCS)_2$-C_2H_2 trimer in the microwave region [23]. The determined geometry was found to be a twisted barrel structure with no symmetry in which the OCS dimer unit resembles the polar OCS dimer as shown in Figure 1-4 (a). On the other hand, distributed multi-pole calculations, indicated that the minimum energy isomer should be a structure having an

antiparallel nonpolar OCS dimer unit, as seen in Figure 1-4 (b). This calculation also showed that the minimum energy isomer should lie at a somewhat lower energy (by ~ 40 cm^{-1}) compared to the observed trimer [23]. Observations in mid-infrared region revealed that the minimum energy structure has indeed a non-polar OCS dimer subunit in which the C_2 symmetry axis is perpendicular to and passing through the center of mass of C_2H_2 [24]. The absence of the minimum energy isomer in the microwave spectra might then be explained by a small or zero permanent dipole moment.

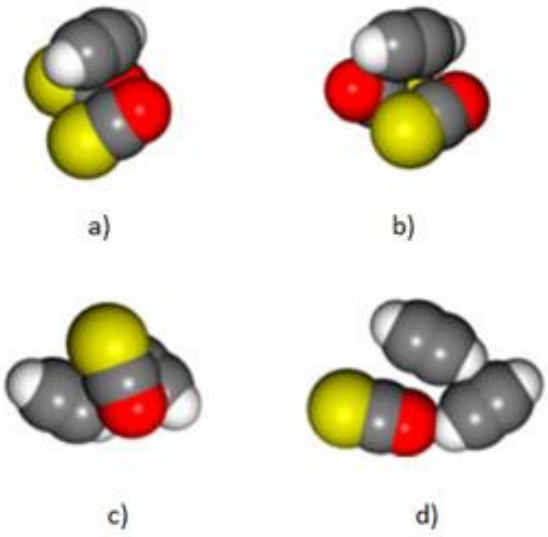

Figure 1-4: The two lowest energy isomers of $(OCS)_2$-C_2H_2 and OCS-$(C_2H_2)_2$: (a) a higher energy isomer of $(OCS)_2$-C_2H_2 having a polar OCS dimer unit; (b) the most stable isomer with C_2 symmetry and a non-polar OCS dimer unit; (c) a higher energy isomer of OCS-$(C_2H_2)_2$with a twisted-barrel structure; (d) the most stable planar isomer [27].

The other possible mixed trimer of C_2H_2 and OCS, OCS-$(C_2H_2)_2$, was also observed in the microwave region [25]. Spectra from the four isotopic forms of the OCS-$(C_2H_2)_2$ trimer (the normal isotope and trimers with $^{13}C_2H_2$, $O^{13}CS$, ^{18}OCS) and semi-empirical modeling resulted in an

asymmetrical barrel-shaped structure, in which the OCS monomer is located "above" the plane of the acetylene dimer. As shown in Figure 1-4 (c), the acetylene dimer unit forms an almost planar structure, between T-shaped and parallel arrangements.

Some experimental anomalies in the microwave observation were addressed by *ab initio* calculation [26]. These anomalies were attributed to large amplitude motions of the C_2H_2 monomers within the dimer unit. The calculations showed that the minimum energy isomer has a planar structure with a nearly T-shaped C_2H_2 dimer subunit with the OCS monomer parallel to the stem of the T. This planar isomer, Figure 1-4 (d), was observed in 2011 by Norooz Oliaee et al. in the mid-infrared region [27]. A question not answered yet is why only the barrel-shaped structure and not the planar isomer is observed in the microwave region.

Recently, Sheybani-Deloui et al. performed semi-empirical calculations on the mixed trimers formed from N_2O and C_2H_2 by [28-30]. These calculations were based on distributed multi-pole pair potentials and using the Powell method to find the global and the local energy minima [31]. It was found that the two lowest energy isomers of $(N_2O)_2$-C_2H_2 and N_2O-$(C_2H_2)_2$, the global and the next higher energy minimum, are analogs of the previously observed lowest energy forms of $(OCS)_2$-C_2H_2 and OCS-$(C_2H_2)_2$ trimers. They observed and reported the minimum energy isomers of $(N_2O)_2$-C_2H_2 and N_2O-$(C_2H_2)_2$ in the region of the ν_1 fundamental band of the N_2O monomer (~2224 cm^{-1}) [30].

1.4 Outline of the thesis

By studying binary and ternary clusters containing "CO_2 family" with acetylene it can be concluded that they are similar in terms of stationary configurations. For instance, mixed trimers formed form N_2O and OCS with acetylene have similar structures. In this study, we address a

question regarding the stationary forms of dimers and trimers formed from CS_2 and C_2D_2. Since these complexes had not been studied previously, there was a need for a theoretical investigation ahead of experimental observations. Chapter 2 contains an introduction to the theoretical background relevant to the study of these complexes. The molecular Hamiltonian is introduced and DFT and rigid rotor-harmonic oscillator approximation as solutions to the molecular Hamiltonian are presented. A DFT method is employed to find the theoretical configuration of stationary complexes using Gaussian 09 package. Experimental observations are also analyzed based on the rigid rotor-harmonic oscillator approximation with the aid of the PGOPHER program. In Chapter 3, the experimental setup used for the spectroscopic observation of the complexes is discussed. The experimental system consists of three parts: 1) Supersonic jet expansion apparatus, 2) Light source and optical devices and 3) data acquisition. In Chapter 4 the results of the theoretical investigations followed by the experimental observations are given. It also includes some concluding remarks with a few suggestions for future work.

Chapter Two: Theoretical background

In this chapter, the required theoretical background to study CS_2 and C_2D_2 binary and ternary complexes is outlined briefly. The Molecular Hamiltonian is presented and solutions to the molecular Hamiltonian are derived. Density Functional Theory is introduced as a computational modeling method to predict the lowest energy isomers. Subsequently, the rigid rotor-harmonic oscillator approximation which gives the lowest order approximation of the molecular Hamiltonian is presented. This approximation is used to analyze the observed spectra. Finally, energy levels for asymmetric top molecules and statistical weights are discussed.

2.1 Molecular Hamiltonian

Molecules are combination of nuclei and electrons, held together by the competition of attractive and repulsive forces in a stationary state with a total energy of E. Theoretically, molecular Hamiltonian and Schrödinger equation can be derived by appropriate transformation of the classical Hamiltonian to a quantum mechanical one [32]. The total molecular Hamiltonian in the space fixed frame is:

$$\hat{H} = \hat{T}_{elec} + \hat{T}_{\mathrm{nuc}} + \hat{\mathrm{V}} \tag{2.1}$$

Where $\hat{T}_{elec}$ shows the kinetic energy of the electrons, $\hat{T}_{nuc}$ the kinetic energy of atomic nuclei. $\hat{\mathrm{V}}$ represents the potential energy which is sum over all the interaction energies of all pairs of particles in the molecule.

$$\hat{\mathrm{V}} = \sum_{S<S'} \hat{V}_{SS'} \tag{2.2}$$

Subsequently, the total energy of the molecular system is found by solution to the time-independent Schrödinger equation:

$$\hat{H}\,\psi = E\,\psi \tag{2.3}$$

However, the analytical or numerical solution of the time-independent Schrödinger equation would be very difficult even for the simplest molecules. To overcome this problem some approximations must be used. In the first step, by choosing the centre of the mass as the origin of the coordinate system, the molecular Hamiltonian can be separated into two parts as:

$$\hat{H} = \hat{T}_{CM} + \hat{H}_{int} \tag{2.4}$$

In which $\hat{T}_{cm}$ donates the kinetic energy of the translational motion of the centre of the mass and $\hat{H}_{int}$ is the Hamiltonian due to the internal degrees of freedom within the molecule. As a result, the wavefunction and the total energy are given by:

$$\psi = \psi_{CM}\psi_{int} \tag{2.5}$$

$$E = E_{CM} + E_{int} \tag{2.6}$$

In the absence of external fields, the translational part can be ignored, because infrared spectroscopy only deals with rotational and vibrational states of molecules and complexes. Thus, the Schrödinger equation is written as:

$$\hat{H}_{int}\psi_{int} = E_{int}\psi_{int} \tag{2.7}$$

In the next step, *Born-Oppenheimer or adiabatic approximation* is applied in order to separate the nuclear and electronic coordinates. Electrons have a light mass, therefore they can move much faster than the vibrating nuclei. Thus we can assume that electronic and nuclear motions are independent of each other. As a result:

$$\hat{H}_{int} = \hat{H}_{nuc} + \hat{H}_{elec} \tag{2.8}$$

$$\psi_{int} = \psi_{\text{nuc}}\ \psi_{elec} \tag{2.9}$$

Using the Born-Oppenheimer approximation, we can assume that the nuclear motion can be ignored, hence the electronic wavefunction is given by:

$$\widehat{H}_{elec}\,\psi_{elec} = E_{elec}\ \psi_{elec} \tag{2.10}$$

E_{elec} includes the electrons-nuclei and electrons-electrons interactions. The electronic structure of an arbitrary molecule or complex can be found by solution to the equation (2.10). In the following sections DFT methods and rigid rotor-harmonic oscillator approximation as solutions to the molecular Hamiltonian are discussed in more detail.

2.2 Density Functional Theory

2.2.1 Hartree-Fock approach

For any arbitrary atom or molecule with N nucleii and M electrons, the Hamiltonian can be written as:

$$\widehat{H}_{elec} = -\sum_{i=1}^{N}\frac{1}{2}\nabla_i^2 - \sum_{i=1}^{N}\sum_{k=1}^{M}\frac{Z_k}{R_{ik}} + \sum_{i=1}^{N}\sum_{i<j}^{N}\frac{1}{r_{ij}} \tag{2.11}$$

In which, the first term is due to the kinetic energy operator of electrons whereas the second term gives the interaction of electrons with nuclei, where Z_k is the charge unit of nucleus k. The lasts gives the electron-electron repulsion. Note that in this equation atomic units are used. The solution to the corresponded Schrödinger equation is:

$$\widehat{H}_{elec}\,\psi_{elec} = E_{elec}\psi_{elec} \tag{2.12}$$

However, solution to equation (2.12) would be so complicated even for simple molecules to find exact wavefunctions. Instead, variational theorem states that the expectation value for the energy of any trial wavefunction for this equation is an upper bound to the true ground state energy

called E_0. Consequently, the exact solution can be found by minimizing the expectation energy with respect to a trail wavefunction. The Hartree-Fock (HF) approach assumes a trial form of the N-electron wavefunction and uses the variational theorem to obtain an approximate solution. In this approximation, the assumed wavefunction is written as the determinant of one-electron function called *Slater determinant*. Where $\psi_i(\vec{x})$ is the probabilistic interpretation of the wavefunction which is function of spin coordinates of all electrons and their spatial variables.

$$\psi_{elec}(1,2,\dots,N) = \begin{vmatrix} \psi_1(\overrightarrow{x_1}) & \psi_2(\overrightarrow{x_1}) & \dots & \psi_N(\overrightarrow{x_1}) \\ \psi_1(\overrightarrow{x_2}) & \psi_2(\overrightarrow{x_2}) & \dots & \psi_N 1(\overrightarrow{x_2}) \\ \vdots & \vdots & \ddots & \vdots \\ \psi_1(\overrightarrow{x_N}) & \psi_2(\overrightarrow{x_N}) & \dots & \psi_N(\overrightarrow{x_N}) \end{vmatrix} \tag{2.13}$$

By substitution of the *Slater determinant* as a trial wavefunction into the Hamiltonian, the following expression for the expectation energy is obtained:

$$E_{HF} = \sum_{i=1}^{N} H_i + 1/2 \sum_{i=1}^{N} \sum_{j=1}^{N} (J_{ij} - K_{ij}) \tag{2.14}$$

H_i gives the kinetic energy and the electron-nucleus attraction as:

$$H_i = \int \psi_i^*(\vec{x}) \left[-\frac{1}{2} \nabla_i^2 - \sum_{k=1}^{M} \frac{Z_k}{R_{ik}} \right] \psi_i(\vec{x})\, d\vec{x} \tag{2.15}$$

J_{ij}, coulomb interaction, defines the electrostatic repulsion between electrons whereas the exchange interaction,K_{ij}, are given by:

$$J_{ij} = \int \psi_i(\overrightarrow{x_1})\, \psi_i^*(\overrightarrow{x_1}) \left[\frac{1}{r_{12}} \right] \psi_j^*(\overrightarrow{x_2})\, \psi_j(\overrightarrow{x_2})\, d\overrightarrow{x_1}\, d\overrightarrow{x_2} \tag{2.16}$$

$$K_{ij} = \int \psi_i^*(\overrightarrow{x_1})\, \psi_i(\overrightarrow{x_1}) \left[\frac{1}{r_{12}} \right] \psi_j(\overrightarrow{x_2})\, \psi_j^*(\overrightarrow{x_2})\, d\overrightarrow{x_1}\, d\overrightarrow{x_2} \tag{2.17}$$

By application of variational theorem to energy expression, Hartree-Fock deferential equations are achieved. The obtained equations are solved iteratively using matrix algebra to find the orbital energies.

2.2.2 Introduction to Density Functional Theory

There is a wide range of methods used in computational chemistry, among which DFT has a good accuracy without an additional increase in computing time. Initially, DFT was introduced in two papers in the 1960's by Hohenberg-Kohn and Kohn-Sham [33, 34]. In the last 30 years, this method has been known as one of the most successful methods in computational chemistry. DFT has been widely used in a broad range of physical and chemical applications to investigate molecular structures, vibrational frequencies, electric and magnetic properties, complexation and ionization energies of molecules, materials and defects. In many cases the results of DFT calculations such as structural determination do agree quite well with experimental data. DFT derives properties of the molecule based on a determination of the electron density. In particular, DFT is a functional of electron density. A functional is a mathematical operation that depends on the entire behavior of a function, not only its value at a specific point. In DFT calculations, the functional is the electron density which is a function of spatial variables. There are still difficulties in using DFT to properly describe intermolecular interactions, especially van der Waals forces, global PES and etc. New DFT methods are developed to overcome these problems by modification of the functionals such as the hybrid functional which will be discussed in the following section.

2.2.3 Electron density

Electron density determines the probability of finding any of the N electrons within a volume element. For a set of N orthonormal one-electron function, ψ_i, the electron density expression is [35]:

$$\rho(\vec{r}) = \sum_{i=1}^{N} \left|\psi_i(\vec{r})\right|^2 \tag{2.18}$$

Note that:

$$N = \int \rho(\vec{r})\, d\vec{r} \tag{2.19}$$

Some properties of the electron density are: 1) electron density is a non-negative function of only the three spatial variables (x, y, z). 2) It vanishes at infinity and integrates to the total number of electrons. 3) It is also an observable function which can be measured experimentally. 4) Last but not least, electron density decays exponentially for large distances from the nuclei. The Hohenburg-Kohn theorem asserts that if the electron density is known, the total energy of the system can be determined. In other words, the electron density uniquely determines the Hamiltonian operator and then all the ground-state properties of the system.

2.2.4 The ground state energy of a poly-electronic system

As it was discussed in previous sections the ground state energy of a poly-electronic system is determined by a functional of the electron density as:

$$E = E_0[\rho(\vec{r})] \tag{2.20}$$

In which the brackets indicate that E_0 is a functional. Based on Kohn-Sham theory, the ground state energy of a molecule with M atomic nuclei and N electrons in a stationary state is written as [35]:

$$E[\rho(\vec{r})] = T_S[\rho(\vec{r})] + V_{ne}[\rho(\vec{r})] + J[\rho(\vec{r})] + E_{XC}[\rho(\vec{r})] \tag{2.21}$$

The first term gives the kinetic energy of the electrons which is an equivalent system of non-interacting electrons. The second term indicates the interaction of the electrons with external potentials, in this case their interactions with the nuclei. The third term, gives the classical electron-electron repulsive interactions. The last term, E_{XC}, is called the exchange-correlation functional that contains every unknown term. It includes exchange and correlation effects, in addition to the difference between the true kinetic energy and the non-interacting kinetic energy. Thus:

$$\begin{aligned} E[\rho(\vec{r})] = & -\frac{1}{2}\sum_{i=1}^{N}\int \psi_i(\vec{r})\left(\nabla^2\right)\psi_i^*(\vec{r})d\vec{r} \\ & + \frac{1}{2}\sum_{i=1}^{N}\sum_{j=1}^{N}\int\int |\psi_i(\vec{r})|^2 \left[\frac{1}{\overrightarrow{r_{12}}}\right] |\psi_i(\vec{r})|^2 \, d\overrightarrow{r_1} d\overrightarrow{r_2} \\ & - \sum_{i=1}^{N}\int \sum_{j=1}^{M}\left[\frac{Z_j}{\overrightarrow{r_{1J}}}\right] |\psi_i(\vec{r})|^2 d\overrightarrow{r_1} + E_{XC}[\rho(\vec{r})] \end{aligned} \tag{2.22}$$

Roughly, there are three different methods to approximate the exchange-correlation functional. 1) Local Density Approximation (LDA) methods which assume that the electron density of the molecule is uniform throughout the molecule. 2) Generalized Gradient Approximation (GGA) methods that depend on the electron density and its gradient in order to account for deviations from uniformity in molecular systems. 3) Hybrid methods which attempt to combine HF approximation with DFT functionals to the exchange-correlation functional.

Choosing the functional depends on the system, the investigated properties, availability and the computational costs. However, in the determination of a geometry optimization hybrid methods provide high levels of accuracy. Hybrid methods, such as Becke 3-term Lee,Yang, and Parr (B3LYP) exchange functional, are commonly used for high accuracy computational chemistry

investigations [36-39]. B3LYP is a combination of local density approximation (LDA), Hartree-Fock (HF), Becke-1988 (B88), Lee-Yang-Parr 1988 (LYP88), and Vosko, Wilks, Nusair 1980 (VWN80) functional. The non-Coulomb part of the exchange functionals typically dies off rapidly. Thus, at large distances it becomes very inaccurate. Handy and coworkers' long range corrected version of B3LYP (CAM-B3LYP) has been used to handle such cases [40]. In this study CAM-B3LYP and also MP2 methods are used to find the theoretical structures.

2.2.5 Minimizing the electron density functional

To solve for $\rho(\vec{r})$ using the functional energy, one must use the variational principle to minimize the energy. The variational theorem states that the expectation value for the energy of any trial wavefunction, is an upper bound to the true ground state energy called E_0. Thus, the approcimate solution of Schrödinger equation can be found by minimizing the expectation energy with respect to a trial solution. By Application of the variational principle, we get:

$$\frac{\delta}{\delta\rho(\vec{r})}\left[E[\rho(\vec{r})] - \mu\int \rho(\vec{r})dr\right] = 0 \qquad (2.23)$$

In which μ is a Lagrange multiplier that ensures that $\int \rho(\vec{r})d\vec{r} = N$. The Kohn-Sham equation is the result of evaluating the functional minimization using equation (2.18) for the electron density [33, 34].

$$(\frac{-\nabla_1^2}{2} + [-\sum_{k=1}^{M}\frac{Z_k}{\overrightarrow{r_{1k}}} + \int\frac{\rho(\overrightarrow{r_2})}{\overrightarrow{r_{12}}}dr_2 + \frac{\delta E_{XC}[\rho(\vec{r}_1)]}{\delta\rho(\vec{r}_1)}]\psi_i(\vec{r}_1) = \epsilon_i\,\psi_i(\vec{r}_1) \qquad (2.24)$$

This equation must be solved self-consistently using following procedure

1. An initial approximation for $\rho(\vec{r})$ is guessed.
2. The Kohn-Sham equation, equation (2.24), is used to derive a set of orbitals $\psi_i(\vec{r})$ and orbital energies $\epsilon_i(\vec{r})$.

3. The derived orbitals are used to update the electron density.
4. The process is iterated at step 2 until the density converges.

This iterative process is complicated and time consuming, so it cannot be done manually. Fortunately, advances in computational chemistry methods have made it possible to perform complicated calculations. Among the wide range of computational software, Gaussian 09 is one of the most utilized software.

2.2.6 Application of DFT using Gaussian 09

Gaussian 09 (G09) is a computational chemistry software which is used for electronic structure modeling [41]. Gaussian 09 does the geometry optimization for a desired molecule or complex by attempting to find the configuration with minimum energy. Initially, the wave function and the energy at a starting geometry are calculated and the calculation then proceeds to search for a new geometry with a lower energy. This process is repeated until the result converges to the lowest energy geometry. It should be noted that this procedure will not necessarily find the global minimum.

In principle, Gaussian approximates orbital shapes and energies of a given molecular geometry using a chemical model. This model consists of two parts: method and basis set. DFT method using CAM-B3LYP functional is chosen as the method for the calculations in this study. A basis set is a set of wave functions that describes the shape of Atomic Orbitals (AOs).The accuracy level of the approximation is directly related to the size of basis set used. Slater Type Orbitals (STOs) and Gaussian Type Orbitals (GTOs) are two types of basis sets used to describe AOs. They are optimized at a Hartree-Fock level which might not be the best for correlated computations. Thom Dunning created a basis set using correlated wavefunctions denoted as cc-pVXZ [42]. cc indicates

that it is a correlation-consistent basis, pV indicates that it is a polarized valence basis, and XZ = shows the zeta number (X is replaced by D for double, T for triple, Q for quadruple). Zeta controls the width of the orbital. The prefix aug- is used to add the diffuse functions [43]. Larger basis sets are more accurate because they are less restrictive on the location of the electrons. However, such calculations are also more expensive in time because they require computing more integrals. Thus, the choice should be made as a trade-off between accuracy of results and CPU usage.

2.3 Rigid rotor-harmonic oscillator approximation

2.3.1 Introduction to rigid rotor-harmonic oscillator approximation

To treat the experimental data, a rigid rotor-harmonic oscillator approximation must be employed for solving the Schrödinger equation. In this lowest order of approximation, the molecular system is treated as a rigid rotor and vibrational motions are modeled by harmonic oscillators. There are 3N-6 independent harmonic oscillators for nonlinear molecules and 3N-5 for linear ones. Thus, for molecules in a singlet electronic ground state with unresolved hyperfine structures Schrödinger equation is written as:

$$\hat{H}_{rv}\,\psi_{rv} = E_{rv}\,\psi_{rv} \tag{2.25}$$

$\hat{H}_{rv}$ is called rotational-vibrational (ro-vibrational) Hamiltonian. Using the rigid rotor-harmonic oscillator approximation, the ro-vibrational Hamiltonian is separated into two parts which are rotational and vibrational parts. Usually, the ro-vibrational Hamiltonian is expressed in terms of the total angular momentum operator $\hat{J}$, normal coordinates $\hat{Q}_r$ and their conjugate momenta $\hat{P}_r$ as [44, 45]:

$$\hat{H}_{rv} = \frac{1}{2}\sum_{\alpha}\mu^{e}_{\alpha\alpha}\hat{J}^2_{\alpha} + \sum_{r}^{3N-6}\frac{1}{2}\left(\hat{P}^{\,2}_{r} + \lambda_r\hat{Q}^{\,2}_{r}\right) = \hat{H}_{rot} + \hat{H}_{vib} \tag{2.26}$$

Where α adopts values of x, y, and z and μ is related to the moment of inertia. The solution of the Schrödinger equation is:

$$(\hat{H}_{rot} + \hat{H}_{vib})\,\psi_{rv} = E_{tot}\,\psi_{rv} \tag{2.27}$$

$$\psi_{rv} = \psi_{rot}\,\psi_{vib} \tag{2.28}$$

and

$$E_{tot} = E_{rot} + E_{vib} \tag{2.29}$$

To refine the ro-vibrational energy levels, some higher order terms called centrifugal distortion also must be taken into account. For instance nonrigidity of molecular structure and anharmonicity of potential are modeled by higher order terms in the molecular Hamiltonian. In the following sections each part of ro-vibrational Hamiltonian will be explained in detail.

2.3.2 Rigid-rotor Hamiltonian

The classical kinetic energy expression for a rigid rotor is given by:

$$E_K = 1/2\;\omega^t I \omega \tag{2.30}$$

ω is the angular velocity vector and I is the inertial moment tensor of a rigid body in 3 dimension shown by a 3×3 tensor as:

$$[I] = \begin{bmatrix} I_{xx} & I_{xy} & I_{xz} \\ I_{yx} & I_{yy} & I_{yz} \\ I_{zx} & I_{zy} & I_{zz} \end{bmatrix} \tag{2.31}$$

where:

$$I_{ii} = \sum_n m_n(j_n^2 + k_n^2) \text{ for } i,j,k \in \{x,y,z\} \tag{2.32}$$

and off-diagonal elements are

$$I_{ij} = -\sum_n m_n i_n j_n \text{ for } i \neq j \in \{x,y,z\} \tag{2.33}$$

This 3×3 tensor can be diagonalized to yield three eigenvalues as followings:

$$I = \begin{bmatrix} I_x & 0 & 0 \\ 0 & I_y & 0 \\ 0 & 0 & I_z \end{bmatrix} \tag{2.34}$$

These diagonal elements are called principal moments of inertia. The energy equation is:

$$E_K = \frac{J_x^2}{2I_x} + \frac{J_y^2}{2I_y} + \frac{J_z^2}{2I_z} \tag{2.35}$$

where J_i^2 is a component of total angular momentum and I_i is the moment of inertia about each axis, respectively. The principle moment of inertia are often labeled as ($I_a \leq I_b \leq I_c$). Therefore, there are six different of relating x, y, z axes to a, b, c axes which are shown in the Table 2-1. Superscripts *r* and *l* refer to right-handed or left-handed coordinate systems, respectively.

Table 2-1: Different representation of the x, y, z axes with the a, b, c axes.

	I^r	II^r	III^r	I^l	II^l	III^l
X	*B*	*C*	*A*	*C*	*A*	*B*
Y	*C*	*A*	*B*	*B*	*C*	*A*
Z	*A*	*B*	*C*	*A*	*B*	*C*

According to the values of the principal moment of inertia components, rigid rotors are categorized into four groups:

I. Linear molecules, ($I_a = I_b, I_c = 0$).

II. Symmetric tops, 1) Oblate symmetric top ($I_a = I_b < I_c$). 2) Prolate symmetric top ($I_a < I_b = I_c$).

III. Spherical tops, ($I_a = I_b = I_c$).

IV. Asymmetric tops, ($I_a \neq I_b \neq I_c$).

By application of quantum mechanics postulates to the classical term of energy, equation (2.30), rotational Hamiltonian of a freely rotating rigid body about the principal axes is obtained as:

$$\widehat{H}_{rot} = \frac{1}{2}\sum_{\alpha} \mu^{e}_{\alpha\alpha} \hat{J}^2_{\alpha} = \hbar^{-2}(A\,\hat{J}^2_a + B\,\hat{J}^2_b + C\,\hat{J}^2_c) \tag{2.36}$$

in which

$$A = \frac{\hbar}{4\pi I_a} \qquad B = \frac{\hbar}{4\pi I_b} \qquad C = \frac{\hbar}{4\pi I_c} \tag{2.37}$$

Where A, B and C are called rotational constants. These constants are in order of $A \leq B \leq C$. In the spectroscopic perspective, if enough rotational constants are known for a given molecule and its isotopologues, then the structure of the molecular species can be determined.

2.3.3 Commutators of the angular momentum operators

To solve the ro-vibrational Hamiltonian two frames should be introduced. These frames are the space fixed frame or (*X*, *Y*, *Z*) and the molecular fixed frame or (*x*, *y*, *z*). In each frame, the magnitude of angular momentum remains constant:

$$J^2 = J_x^2 + J_y^2 + J_z^2 = J_X^2 + J_Y^2 + J_Z^2 \tag{2.38}$$

It can be shown by math that:

$$\left[\hat{J}_i, \hat{J}_j\right] = i\sum_{k} \epsilon_{ijk} J_k \qquad and \quad i,j,k \in \{X,Y,Z\} \tag{2.39}$$

$$\left[\hat{J}_l, \hat{J}_m\right] = -i\sum_{n} \epsilon_{lmn} J_n \quad and \quad l,m,n \in \{x,y,z\} \tag{2.40}$$

where:

$$\epsilon_{abc} = \begin{cases} +1\ for\ even\ permutaiotion\ of\ a,b,c \\ -1\ for\ odd\ permutaiotion\ of\ a,b,c \\ 0 \qquad\qquad\qquad\qquad otherwise \end{cases} \tag{2.41}$$

and commutation relations between these operators are:

$$\left[\hat{J}_i, \hat{J}_l\right] = 0 \qquad \left[\hat{J}^2, \hat{J}_l\right] = 0 \qquad \left[\hat{J}^2, \hat{J}_i\right] = 0 \tag{2.42}$$

Using these commutation relations, we get:

$$\left[\widehat{H}_{rot}, \hat{J}^2\right] = \left[\widehat{H}_{rot}, \hat{J}_Z\right] = 0 \tag{2.43}$$

And

$$[\hat{H}_{rot}, \hat{J}_z] = i\left(\frac{1}{2I_x} - \frac{1}{2I_y}\right)(\hat{J}_x\hat{J}_y + \hat{J}_y\hat{J}_x) \tag{2.44}$$

Since $\hat{J}^2$, $\hat{J}_Z$ and $\hat{J}_z$ form a commuting set of operators, they share a common set of eigenfunctions denoted as $|J, k, m\rangle$ with the following eigenvalues:

$$\hat{J}^2|J, k, m\rangle = \hbar^2 J(J+1)|J, k, m\rangle \tag{2.45}$$

$$\hat{J}_z|J, k, m\rangle = \hbar k|J, k, m\rangle \tag{2.46}$$

$$\hat{J}_Z|J, k, m\rangle = \hbar m|J, k, m\rangle \tag{2.47}$$

J, k and m are the quantum numbers associated with $\hat{J}^2$, $\hat{J}_z$ and $\hat{J}_Z$, respectively. These quantum numbers can assume the following values:

$$J = 0, 1, 2, \ldots \tag{2.48}$$

$$k = 0, \pm 1, \ldots, \pm J \tag{2.49}$$

$$m = 0, \pm 1, \ldots, \pm J \tag{2.50}$$

2.3.4 Rotational energy levels of asymmetric top molecules

For a symmetric top, two of the principal moments of inertia are equal and the third is non-zero. Thus $\hat{J}_a$ or $\hat{J}_c$ comute with the rotational Hamiltonian as well [44]:

$$[\hat{H}_{rot}, \hat{J}_a] = 0 \text{ for oblate top} \tag{2.51}$$

$$[\hat{H}_{rot}, \hat{J}_c] = 0 \text{ for prolate top} \tag{2.52}$$

Energy levels of oblate and prolate symmetric tops can be obtained as:

$$E_p = (A - B)k_a^2 + BJ(J+1) \tag{2.53}$$

$$E_o = (C - B)k_c^2 + BJ(J+1) \tag{2.54}$$

For a specific *J*, as the k_a increases, the energy increases for a prolate top whereas the energy of an oblate top decreases as k_c increases. Solution to the asymmetric top rotational Hamiltonian,

except for low J, is not possible analytically due the fact that $\left[\widehat{H}_{rot}, \hat{J}_z\right] \neq 0$. However, the symmetric top basis, prolate or oblate, can be used to obtain the rotational energies for the asymmetric top. To do so, the asymmetric top ladder operators are introduced in the molecular fixed frame. Choosing I^r representation and prolate top symmetric wavefunctions $|J, k_a, m\rangle$, the ladder operators in the molecular and space fixed frames are:

$$\hat{J}_m^{\pm} = \hat{J}_b \pm i\hat{J}_c \tag{2.55}$$

$$\hat{J}_s^{\pm} = \hat{J}_X \pm i\hat{J}_Y \tag{2.56}$$

with the following commutation relation:

$$[\hat{J}_a, \hat{J}_m^{\pm}] = \mp \hat{J}_m^{\pm} \tag{2.57}$$

$$[\widehat{J}_Z, \hat{J}_s^{\pm}] = \pm \hat{J}_s^{\pm} \tag{2.58}$$

Using the ladder operators, the ro-vibrational Hamiltonian is rewritten as:

$$\widehat{H}_{rot} = \left(\frac{B+C}{2}\right)\hat{J}^2 + \left(A - \frac{B+C}{2}\right)\hat{J}_z^2 + \left(\frac{B-C}{4}\right)\left(\hat{J}_m^{+\,2} + \hat{J}_m^{-\,2}\right) \tag{2.59}$$

Consequently:

$$\hat{J}_m^{\pm}|J, k_a, m\rangle = \sqrt{J(J+1) - k_a(k_a \mp 1)}\,|J, k_a \mp 1, m\rangle \tag{2.60}$$

$$\hat{J}_s^{\pm}|J, k_a, m\rangle = \sqrt{J(J+1) - m(m \pm 1)}\,|J, k_a, m \pm 1\rangle \tag{2.61}$$

As a result, the non-vanishing elements in the rotational Hamiltonian matrix are:

$$\langle J, k_a, m|\hat{J}^2|J, k_a, m\rangle = J(J+1) \tag{2.62}$$

$$\langle J, k_a, m|\,\hat{J}_z^2\,|J, k_a, m\rangle = k_a^2 \tag{2.63}$$

$$\langle J, k_a \mp 2, m|\,\hat{J}_m^{\pm\,2}|J, k_a, m\rangle = \sqrt{J(J+1) - k_a(k_a \mp 1)}\sqrt{J(J+1) - (k_a \mp 1)(k_a \mp 2)} \tag{2.64}$$

Based on these equations $\widehat{H}_{rot}$has non-vanishing matrix elements only between the states of the same J and m and the states with $\Delta k_a = 0, \pm 2$. As an example, for $J = 1$, the Hamiltonian is a 3×3 matrix with $|J = 1, k_a = 1\rangle$, $|J = 1, k_a = 0\rangle$ and $|J = 1, k_a = -1\rangle$ basis wavefunction, thus:

$$\widehat{H} = \begin{array}{c} \\ \langle 1,-1| \\ \langle 1,0| \\ \langle 1,+1| \end{array} \begin{array}{c} \begin{array}{ccc} |1,-1\rangle & |1,0\rangle & |1,+1\rangle \end{array} \\ \begin{bmatrix} A + \frac{B+C}{2} & 0 & \frac{B-C}{2} \\ 0 & B + C & 0 \\ \frac{B-C}{2} & 0 & A + \frac{B+C}{2} \end{bmatrix} \end{array} \tag{2.65}$$

This matrix can be divided into two blocks, a 2×2 block and a 1×1 block, by exchanging rows and columns. Diagonalizing this matrix, one can write:

$$|1,1,O^+\rangle = \frac{1}{\sqrt{2}} (|1,1\rangle + |1,-1\rangle) \tag{2.66}$$

$$|1,1,O^-\rangle = \frac{1}{\sqrt{2}} (|1,1\rangle - |1,-1\rangle) \tag{2.67}$$

$$|1,0,E^+\rangle = |1,0\rangle \tag{2.68}$$

The labels E^+, E^-, O^+ and O^- indicate whether k_a is even or odd, and whether the wavefunctions are formed by + or - linear combination of symmetric top wavefunctions. In this case, the energy levels are the diagonal elements of the Hamiltonian matrix. For the higher J quantum numbers, the same procedure can be applied to derive the energy levels. Thus the Hamiltonian can be written as:

$$\widehat{H} = \begin{array}{c} \\ \langle 1,1,O^+| \\ \langle 1,1,O^-| \\ \langle 1,0,E^+| \end{array} \begin{array}{c} \begin{array}{ccc} |1,1,O^+\rangle & |1,1,O^-\rangle & |1,0,E^+\rangle \end{array} \\ \begin{bmatrix} A + B & 0 & 0 \\ 0 & A + C & 0 \\ 0 & 0 & B + C \end{bmatrix} \end{array} \tag{2.69}$$

2.3.5 Harmonic Oscillator

Vibrational motion of a molecule with N atoms, is modeled by 3N-6 harmonic oscillator (3N-5 for linear molecules) in the lowest order approximation. Each atom has 3 degrees of freedom out of which 3 degrees are reserved for the motion of the center of mass. Moreover, 3 (2 for linear molecules) degrees of freedom are reserved for the rotational motion. Thus, 3N-6(5) degrees remain for vibrational motion. This harmonic oscillator approximation can be applied for small values of vibrational quantum number. Vibrational energy is found by solving harmonic oscillator Schrödinger equation as:

$$\sum_{r}^{3N-6} \frac{1}{2}\left(\hat{P}_r^{\,2} + \lambda_r \hat{Q}_r^{\,2}\right) \psi_{vib}\left(Q_1, Q_2, \dots, Q_{3N-6}\right) = \mathrm{E}_{vib}\psi_{vib}(Q_1, Q_2, \dots, Q_{3N-6}) \tag{2.70}$$

The vibrational wavefunction, for a given molecule, is written as the product $3N-6$ wavefunction, one for each normal coordinate, as:

$$\psi_{vib}(Q_1, Q_2, \dots, Q_{3N-6}) = \psi_{v1}(Q_1)\psi_{v2}(Q_2)\dots\psi_{v(3N-6)}\left(Q_{(3N-6)}\right) \tag{2.71}$$

thus:

$$\frac{1}{2}\left(\hat{P}_r^{\,2} + \lambda_r \hat{Q}_r^{\,2}\right)\psi_{rv}(Q_r) = \mathrm{E}_{vr}\psi_{rv}(Q_r) \tag{2.72}$$

Regarding the solution for one dimensional problem, the vibrational wavefunction and energy for the molecule is [44]:

$$\begin{aligned} \psi_{vib} &= \exp\left[-\frac{1}{2}\sum_{r}^{3N-6}\frac{\omega_r}{\hbar}\,\hat{Q}_r^{\,2}\right]\prod_{r}^{3N-6} N_{vr}H_{vr}\left(\sqrt{\frac{\omega_r}{\hbar}}Q_r\right) \\ E_{vib} &= \sum_{r}^{3N-6}\left(v_r + \frac{1}{2}\right)\hbar\omega_r \end{aligned} \tag{2.73}$$

In which N_{vr} is the normalization factor:

$$N_v = \frac{\left(\sqrt{\omega}\right)}{\sqrt{\hbar\,\pi} 2^v v!} \tag{2.74}$$

2.3.6 Ro-vibrational spectrum and selection rules

Absorption spectrum can be obtained by passing the light source through a gas flow and detecting the radiation. In fact, interaction of wave and dipole moment is observed in the spectrum. If an electromagnetic radiation with an initial intensity of $I_0(\tilde{\nu})$ and wavenumber of $\tilde{\nu}$ is passed through a gas cell with a length of l and concentration of C^*, the transmitted intensity, $I_t(\tilde{\nu})$, is determined by Lambert-Beer law as [44]:

$$I_t(\tilde{\nu}) = I_0(\tilde{\nu})\, \mathrm{e}^{(-lC^*\alpha_{if}(\tilde{\nu}))} \tag{2.75}$$

Where $\alpha_{if}(\tilde{\nu})$, the absorption coefficient, from an initial state with energy E_i to a final state with energy E_f at thermal equilibrium is:

$$\alpha_{if} = \frac{8\pi N_A \tilde{\nu}_{if} \left[\exp\left(-\frac{E_i}{kT}\right) - \exp\left(-\frac{E_f}{kT}\right)\right]}{(4\pi\epsilon_0)3hc^2 Z} S \tag{2.76}$$

In which N_A is the Avogadro number, $\tilde{\nu}_{if} = \frac{E_f - E_i}{hc}$ is the frequency of the transition in cm^{-1}, k is the Boltzmann constant, h is the Planck constant, c is the speed of light, and Z is the partition function. S is the line strength which is defined as:

$$S = \left[\sum_{\alpha=X,Y,Z} |\langle\psi_{rv}^m|\mu_\alpha^s|\psi_{rv}^n\rangle^2|\right] \tag{2.77}$$

μ_α^s (α= *X*, *Y*, *Z*) are the components of electric dipole moment in the space-fixed frame (μ^s). Thus, in an absorption spectrum, intensity of ro-vibrational transitions is proportional to electric dipole moment ($\langle\psi_{rv}^m|\mu_\alpha^s|\psi_{rv}^n\rangle$). Electric dipole moment can be written in terms of its components in the molecule fixed frame as:

$$\mu_\alpha^s = \sum_{i=x,y,z} \lambda_{i\alpha}\, \mu_i^m \tag{2.78}$$

Where $\lambda_{i\alpha}$ are the transformation matrix elements which are dependent on Euler angles. μ_α^m can be expanded in in terms of the normal coordinates about the equilibrium configuration as:

$$\mu_i^m = (\mu_i^m)_{eq} + \sum_k \left(\frac{\partial \mu_i^m}{\partial Q_k}\right)_{eq} Q_k + \cdots \tag{2.79}$$

Thus:

$$\langle \psi_{rv}^m | \mu^s | \psi_{rv}^n \rangle = \langle \psi_{rv}^m | \sum_{i=x,y,z} \lambda_{i\alpha} \left((\mu_i^m)_{eq} + \sum_k \left(\frac{\partial \mu_i^m}{\partial Q_k}\right)_{eq} Q_k + \cdots \right) | \psi_{rv}^n \rangle \tag{2.80}$$

Infrared investigation deals with such cases that the molecular vibration gives rise to a net change in dipole moment of the molecule (second term of equation (2.75)). Thus, for an infrared ro-vibration spectrum and using equation (2.23), we get:

$$\langle \psi_{rv}^m | \mu^s | \psi_{rv}^n \rangle = \sum_{i=x,y,z} \sum_k \left(\frac{\partial \mu_i^m}{\partial Q_k}\right)_{eq} \langle \psi_{vib}^m |\, Q_k | \psi_{vib}^n \rangle \langle \psi_{rot}^m | \lambda_{i\alpha} | \psi_{rot}^n \rangle \tag{2.81}$$

As can be seen in equation (2.83), non-vanishing elements of $\langle \psi_{rv}^m | \mu^s | \psi_{rv}^n \rangle$ matrix are governed with both symmetry of dipole moment operator involved in the transition and the ro-vibrational wavefunctions of the two levels. Thus, all transitions are not possible in the absorption spectrum. The ro-vibrational selection rules for an asymmetric top molecule for vibrational fundamentals are $\Delta v = +1$ and $\Delta J = 0, \pm 1$. Transitions with $\Delta J = -1,\ \Delta J = 0$ and $\Delta J = +1$ are called Q-branch, R-branch and P-branch, respectively. Furthermore, any molecule can have three components of dipole moments along principle axes. Depending on which components of the dipole moment are equal to zero, transitions can be categorized into three types; a-, b- and c-type transitions.

***a*-Type Transitions**: $(\mu_a \neq 0, \mu_b = \mu_c = 0)$. Selection rules for these transitions are:

$$\Delta K_a = 0\,, \Delta K_c = \pm 1 \tag{2.82}$$

result in prominent Q-branch near the band center and the transitions in the parentheses are much weaker.

***b*-Type Transitions**: ($\mu_b \neq 0, \mu_a = \mu_c = 0$). Then, selection rules can be listed as:

$$\Delta K_a = \pm 1\ , \Delta K_c = \pm 1 \tag{2.83}$$

usually result in a clear gap at the center of the ro-vibrational band which has only b-type transitions.

***c*-Type Transitions**: ($\mu_c \neq 0, \mu_a = \mu_b = 0$) thus transition occur with the selection rules as:

$$\Delta K_a = \pm 1\ , \Delta K_c = 0 \tag{2.84}$$

which is similar in appearance as a-type band with a significant $Q-$branch at the center of the spectrum. In general, a molecule may have more than one non-zero components of the dipole moment, thus, two or all three types of transitions can occur together in the spectrum and this is called a "hybrid" band.

2.3.7 Statistical weights

In a given spectrum some features such as intensity alternation, specific intensity patterns, and also missing some levels can be explained by variation of statistical weights of ro-vibrational states. The complete internal wavefunction ψ_{int} is the result of:

$$\psi_{int} = \psi_{rv}\psi_{ns} \tag{2.85}$$

In which ψ_{rv} is ro-vibrational wavefunction and ψ_{ns} is the nuclear spin wavefunction. Based on the Pauli Exclusion Principle ψ_{int} must be invariant under any permutation of the integer spin nuclei, while it must be symmetric (anti-symmetric) under even (odd) permutation of the half integer spin nuclei,

$$P_{(odd)}\psi_{int} = \psi_{int} \text{ for bosons and } P_{(odd)}\psi_{int} = -\psi_{int} \text{ for fermions} \tag{2.86}$$

$$P_{(even)}\psi_{int} = \psi_{int} \qquad \text{for bosons and fermions}$$

Furthermore, effect of E^*or inversion operator on this wavefunction:

$$E^*\psi_{int} = \pm\psi_{int} \tag{2.87}$$

Thus, only those states are populated in which their product with a nuclear spin states symmetry is allowed for the total internal wavefunction.

$$\Gamma_{rve} \otimes \Gamma_{ns} \supset \Gamma_{int} \tag{2.88}$$

There are $\prod_{i=1}^{N}(2I_i + 1)$ spin functions in a molecule with N nuclei, where I_i is nuclear spin of the ith nucleus. The characters generated by the nuclear spin wavefunctions is obtained from [44]:

$$\chi[P] = 2\prod(2I_a + 1)(-1)^{2I_a(n_a-1)}$$
$$\chi[P^*] = 0 \tag{2.89}$$

where the P and P^* are permutation and permutation-inversion operators in the MS group. This product contains one factor for each set of n_a nuclei having spin I_a that are permuted by P or P^*.

2.3.8 PGOPHER program

For simulation of the observed ro-vibrational spectra PGOPHER program is used [46]. This program solves an inverse eigenvalue problem to find the corresponding Hamiltonian. Ro-vibrational constants are varied by fitting transition frequencies to find the Hamiltonian. These parameters are the coefficients of the various terms involving rotational and vibrational angular momenta in the Hamiltonian. Depending on the band, temperature of the sample, line broadening and line shapes, point group symmetry of the molecule, representation of the Hamiltonian, statistical weights, symmetry axes, symmetry of the ground and excited vibrational state and approximate band origin must be provided as the input. The quality of the fit is assessed by the

Root Mean Square (RMS) of observed frequencies and the corresponding calculated frequencies as follows:

$$\Delta v_{rms} = \sqrt{\frac{1}{N}\sum_{i=1}^{N}\left(v_i^{obs} - v_i^{cal}\right)^2} \tag{2.90}$$

The main window of PGOPHER is shown in Figure 2-1. The top trace is observed and the bottom one is simulated spectrum of CS_2-D_2D_2 planar parallel dimer which will be discussed in the fourth chapter.

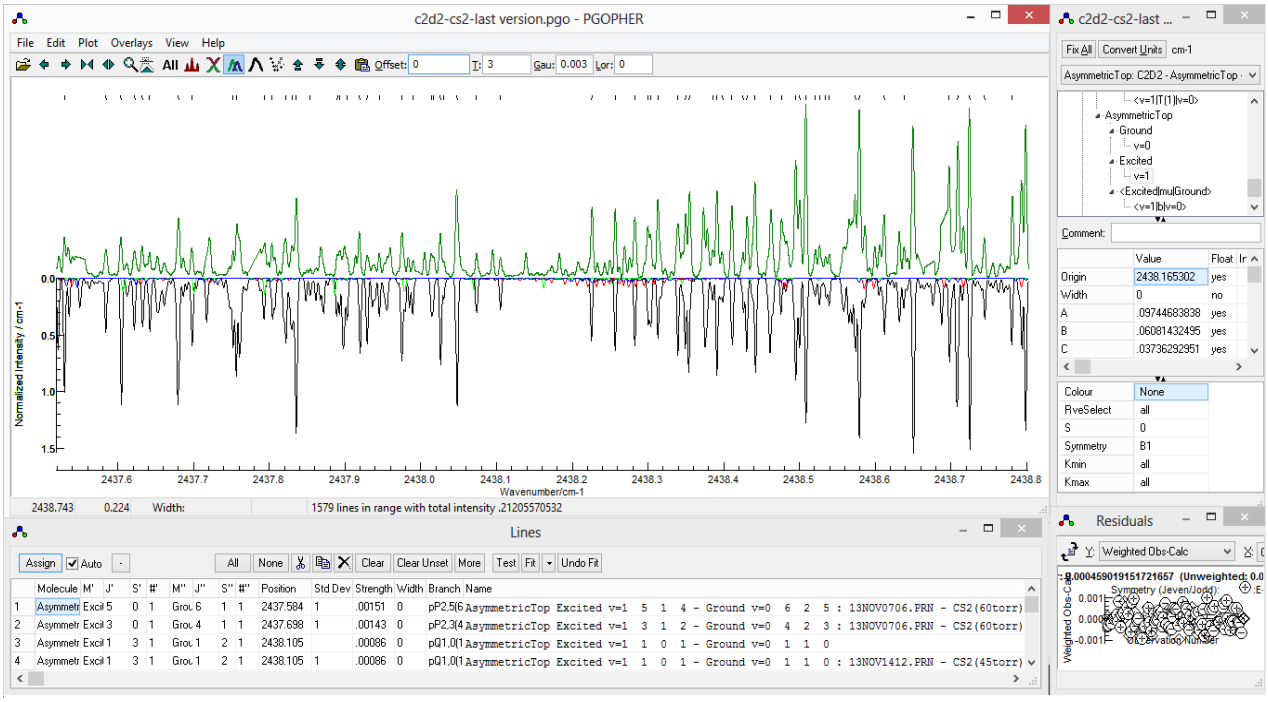

Figure 2-1: Snapshot of PGOPHER front panel used for simulation of the rotational, vibrational and electronic spectra.

Chapter Three: Experimental apparatus

In this chapter, the experimental setup utilized to record the spectra of weakly-bound van der Waals complexes of CS_2 and C_2D_2 are described. This setup, shown in Figure 3-1, consists of three parts. The supersonic jet apparatus and the vacuum system used to generate molecular clusters. Light source and optical components used to probe molecular complexes in the supersonic jet. Finally, the electronic setup used to store and process the recorded data. Briefly, the desired van der Waals complexes are generated in a supersonic slit-jet apparatus and probed by an OPO using a multi-pass absorption cell mounted in the jet chamber. In order to calibrate the recorded spectra, a fixed etalon and a reference gas cell are used. In the following sections, each part will be described in detail.

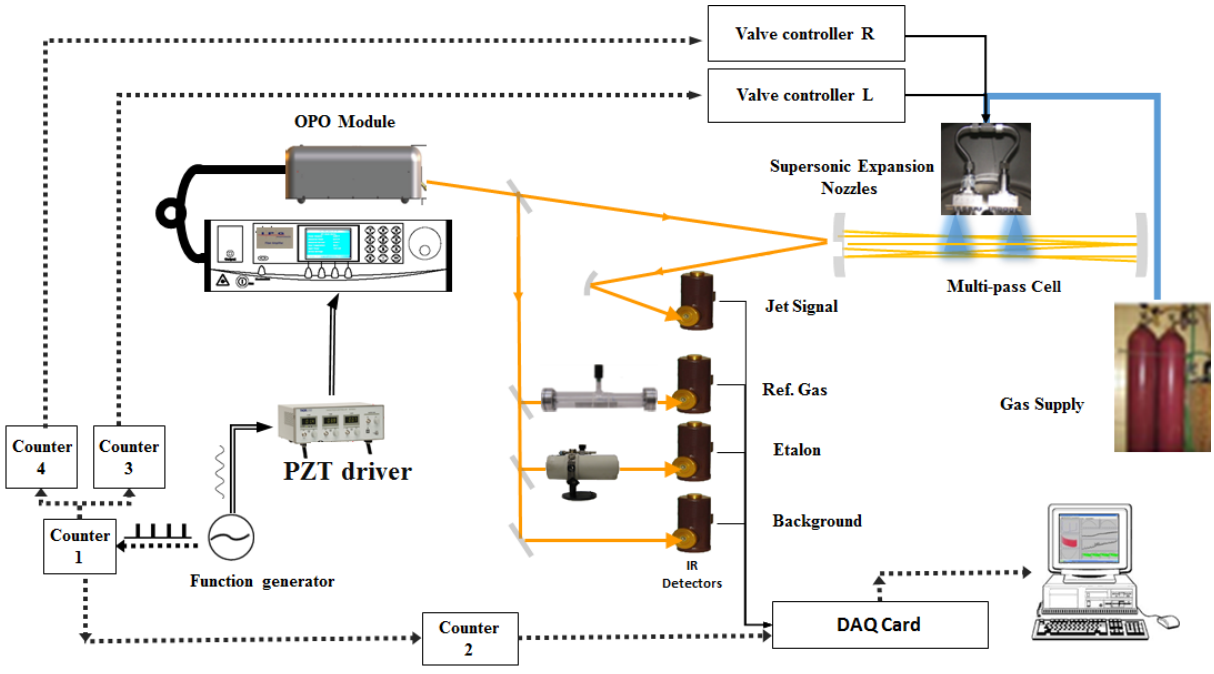

Figure 3-1: Overview of the experimental setup used for spectroscopic study of vdW complexes.

3.1 Supersonic apparatus

3.1.1 Theory of supersonic Jet Expansion

Supersonic jet expansion is the most efficient technique that has been developed to create and study weakly bound van der Waals complexes. A supersonic jet apparatus generates rotationally cold beams of the desired complexes. It also provides a collision-free environment characterized by a very narrow velocity distribution and very low rotational temperatures. Thus, the recorded spectra of complexes are greatly simplified. This process is called supersonic since the gas flow velocity after the expansion exceeds the local speed of sound after the expansion.

A supersonic jet is formed when a high pressure gas mixture, expands into vacuum region through a small orifice. The gas mixture is a buffer gas, such as helium, seeded with a low concentration of the polyatomic species of interest. Inside the high pressure region, molecules move in random directions and undergo many binary collisions. Some of the molecules, because of collisions in the vicinity of orifice, are able to escape into the low pressure region. If the diameter of orifice is much larger than mean-free path of the gas particles, most of the molecules leaving the high pressure region achieve a large velocity in the direction perpendicular to the orifice area. Thus, the distribution of velocity narrows down and the translational temperature is decreased [47].

Once the velocity distribution narrows down, only low energy collisions between polyatomic and carrier gas molecules are possible. Through these collisions, hot polyatomic molecules transfer their vibrational and rotational energies to the translation energy of their partners. The collision-induced rotational transition is smaller than the elastic collision cross-section. Also the collision cross-section for vibration-translation energy transfer is even smaller [48]. Thus, the cooling order is:

$$T_{vib} > T_{rot} > T_{tarns} \tag{3.1}$$

By looking at the energy spacing of translational, rotational, and vibrational levels, this temperature ordering can be well understood. In supersonic expansion, rotational temperatures are in the order of 0.1-10 K while vibrational temperatures are much higher, 20-150 K. in supersonic jet expansions [49]. As the mixture expands into the low pressure region, because of collisions with the background gas molecules, a shock wave is established. This shock wave protects the core of the jet from the warm background gas and provides an ideal region in favour of spectroscopic measurements.

Supersonic expansion can be explained by a hydrodynamic-flow model as well. Cooling process can be treated as an adiabatic process because the expansion occurs so fast and heat exchange cannot occur with its surroundings. By careful choice of expansion conditions, the seed molecule may be prepared in a state in which only the lowest energy rotations are populated [50] Based on the conservation of energy, for a mole of gas with mass $\mathcal{M}$, the total energy before and after the expansion is:

$$U_0 + P_0V_0 + \frac{1}{2}\mathcal{M}u_0^2 = U + PV + \frac{1}{2}\mathcal{M}u^2 \tag{3.2}$$

In this equation the total internal energy is defined as $U = U_{trans} + U_{vib} + U_{rot}$, the potential energy is PV and the kinetic energy is $\frac{1}{2}\mathcal{M}u^2$, where u is the mean flow velocity of the expanding gas [50].With the assumption of thermal equilibrium inside the reservoir, u_0 will be very small and the kinetic-flow energy before the expansion can be neglected. In addition, pressure after the expansion is so small $P \ll P_0$ and the potential energy of the expanded gas can be neglected as well. Thus the equation (3.2) can be rewritten as:

$$U_0 + P_0V_0 = U + \frac{1}{2}\mathcal{M}u^2 \tag{3.3}$$

which shows that most of the initial energy converts into kinetic-flow energy, hence a molecular beam with small internal energy is obtained. This condition is usually described in terms of the Mach number, M, being greater than unity. The Mach number is defined as the ratio of the bulk flow velocity to the local speed of sound.

$$M = \frac{u}{u_s}$$
$$u_s = (\frac{\gamma RT_{tr}}{m})^{1/2} \tag{3.4}$$

In which $\gamma = \frac{C_p}{C_V}$=5/3 is the specific heat ratio for the gas and m is the mass of the gas particles. A schematic diagram of a supersonic expansion beam is depicted in Figure 3-2.

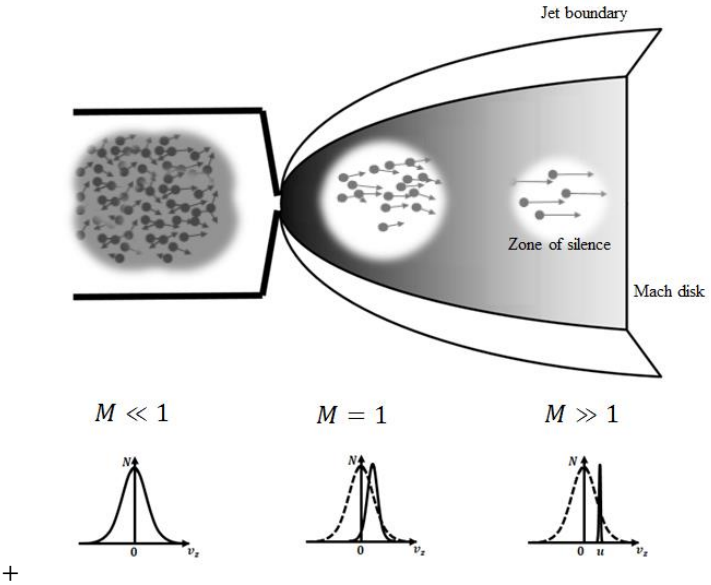

Figure 3-2: Diagram of the supersonic expansion of a gas in a vacuum chamber. Along the expansion, velocity distribution narrows down through the expansion from Gaussians distribution. Velocity distribution are shown in different regions categorized by Mach number.

3.1.2 Supersonic jet chamber and Vacuum pumps

A NW250 six-way cross is used for the jet chamber. The jet is mounted on a Varian VHS-10 diffusion pump for evacuation. This pump is also backed by a rotary vane vacuum pump (Edwards, E2M2750). The pump is located in a separate room at a distance of about 3 meters in order to minimize the transfer of noise and mechanical vibrations. The average gas flow can be monitored using a thermocouple vacuum gauge located in the backing line. Pressure inside the vacuum chamber is also measured by an ionization gauge (Edward Active Inverted Magnetron ionization). The system is capable of maintaining a vacuum as low as 10^{-7} Torr. However, during the jet operation the pressure in the vacuum chamber may reach as high as 10^{-4} Torr. The six way cross and vacuum chamber are shown in Figure 3-3.

Figure 3-3: Photograph of the vacuum system showing the six-way vacuum chamber, diffusion pump, and the pneumatic gate valve in the middle.

3.1.3 Pulsed valves and nozzles

A gas mixture is expanded through the two side-by-side slit nozzles to produce planar supersonic expansions. Slit shape nozzles give much longer optical path lengths and high molecular densities and slow adiabatic cooling [51]. This increases the probability to have two and three-body collisions, hence efficient generation of molecular clusters. Nozzle blocks are attached to pulsed solenoid valves (General Valve Series 9) manufactured by Parker Hannin Corporation. These valves operate in a pressure range of up to 85 atmospheres and the repetition rate can be as high as 125 Hz. Valve controller unit (Ioata one) controls the pulse duration. Pulse duration is optimized for the system depending on the gas mixture. Slit nozzles configuration is shown in Figure 3-4.

Figure 3-4: Dual pulsed slit nozzle valve configuration inside the vacuum chamber

3.2 Probe laser and optical setup

3.2.1 Optical parametric oscillator

To probe the generated complexes, an Optical Parametric Oscillator (OPO) source is used. OPO is a light source which works based on optical gain from parametric amplification in a nonlinear crystal [52, 53]. In an optical parametric process the pump photon ($\boldsymbol{\omega_p}$) is split in two parts, with different energies. The generated photon with the highest energy is called signal ($\boldsymbol{\omega_s}$),

and the other photon is termed idler ($\boldsymbol{\omega_i}$) in which $\boldsymbol{(\omega_s > \omega_i)}$. For the pair of generated photons the energy conservation must be satisfied:

$$\omega_p = \omega_s + \omega_i \tag{3.5}$$

In addition, destructive interference between the created photons needs to be prevented. This results in phase-matching condition as:

$$k_p = k_s + k_i \tag{3.6}$$

OPO light source consists of two main parts, an optical resonator and a nonlinear optical crystal. An OPO with a resonator at either the signal or the idler wavelength is called Singly Resonant OPO (SRO). In the nonlinear optical crystal, there is an interaction between the pump, signal and idler. This interaction leads to amplitude gain for the signal and idler and a de-amplification of the pump. Invention of new crystals like Periodically Poled Lithium Niobate (PPLN) has led to the development of low oscillation threshold SROs.

A valuable advantage of OPO is possibility to access wide ranges (mid-infrared, far-infrared and terahertz spectral region) with wide wavelength tuneability. They are capable of delivering outputs with narrow line-width and high power. Because of these features, OPOs are considered as excellent light sources for spectroscopic applications. Wavelength tuning is accomplished by altering the propagation direction in crystal or changing the crystal temperature.

The light source used in recording the spectra of CS_2 and C_2D_2 is a cw singly resonant OPO (Lockheed Martin Argos Model 2400-Module D). The idler output which is used to probe the complexes has tuning range from 2173 to 2564 cm^{-1}.The OPO cavity resonator is a four-mirror cavity. The front surfaces of the cavity mirrors are highly reflecting at the signal wavelength and highly transmissive at both pump and idler wavelengths. Thus, the light source is SRO at the signal wavelength. The nonlinear crystal is 5% magnesium-oxide doped periodically-poled lithium

niobate (MgO:PPLN), with anti-reflection coating for all the three wavelengths. The OPO pump source is a 10 W, 1064 nm fiber-based laser in a Master Oscillator Power-Amplifier (MOPA) configuration. The seed laser is a cw Yb-doped fiber laser (Koheras Adjustik 000, 1064 nm, 15 mW, <100 kHz). Configuration of OPO module is depicted in Figure 3-5.

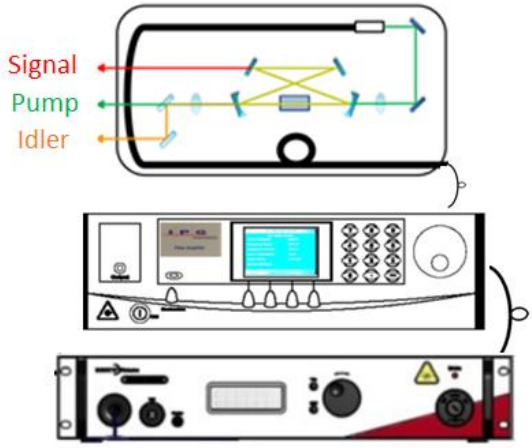

Figure 3-5: Schematic of an OPO module showing the main components.

There are several methods for frequency tuning of the available OPO. Coarse idler frequency tuning is done manually with fine-pitch screw on the top of the module. Continuous idler frequency tuning over a 2 cm^{-1} range is done by application of a signal from external PZT driver (Thorlabs, MDT693B). PZT output with 0-110 voltage range is applied to the seed laser PZT element. Moreover, the crystal is mounted in a temperature controlled oven. The oven stabilizes the temperature anywhere between 45 °C and 70 °C with a precision of 0.1C. Changing the crystal temperature is also used for frequency tuning.

3.2.2 Short term frequency stabilization

Short term frequency drift of OPO is compensated by using the circuit shown in Figure 3-6. In this compensation procedure, a peak of transition line of the reference sample is chosen as the reference point. Any small drift can be visually seen with respect to the reference point. The full

adder circuit adds a DC offset to the scanning sine wave with a range of about -0.1 to 0.1 V. An extra input is also designed for the future usage to do the compensation by a computer program. The drift should be measured by the program and then an error signal is applied to the sine wave to bring the laser back to the marked reference point.

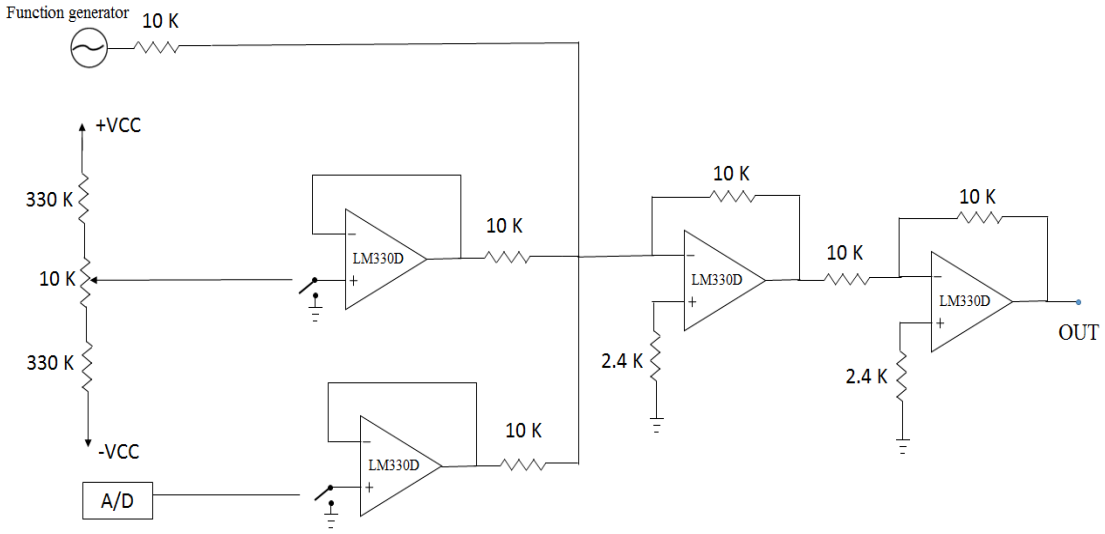

Figure 3-6: The electronic compensation circuit.

3.2.3 Optical setup configuration

Radiation of the OPO is directed to the optical setup by two gold coated flat mirrors. A beam splitter is used to divide the radiation into two parts. 80% of the beam is focused at the centre of the jet to probe the supersonic jet expansion. The weaker part is also divided into three portions using two other beam splitters. Two portions are directed into a reference gas cell and passive etalon for calibration. The reference cell is a glass tube (300 mm length and 45 mm diameter) with two CaF_2 windows at the ends. This cell contains a reference gas (CO_2 or N_2O) with known transition frequencies in the spectral region of interest. The confocal passive etalon is used for frequency interpolation. It has a free spectral range of 0.00997 cm^{-1}. The last portion of the beam is used to record the background signal and suppress OPO power fluctuation.

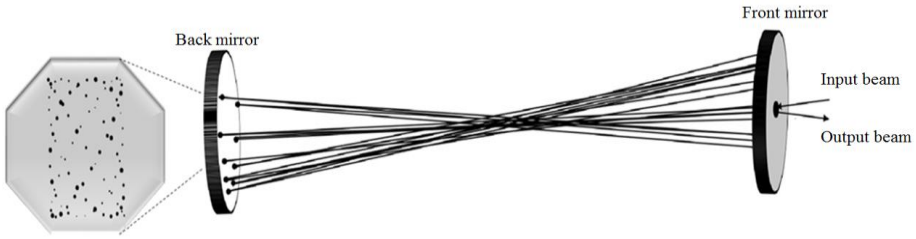

Figure 3-7: Schematic of the absorption cell. Front and back astigmatic mirror with the spot pattern on the back mirror.

3.2.4 Multi-pass Absorption Cell

Increasing the absorption path length is a commonly used technique to obtain spectra with higher signal to noise ratio (SNR). This is needed for recording spectra of weak bands such as combination bands. In order to enhance the sensitivity of the system, a multi-pass absorption configuration (Aerodyne Research Inc., AMAC-100) [54] is mounted inside the jet chamber. This cell consists of two astigmatic mirrors with a reflectivity of 99.2% installed at the ends of a 70 cm long stainless steel base. The beam is circulated inside the cell which effectively increases the absorption path. The multi-pass cell increases the number of laser passes, ranging from 86 to 366, depending on the incident beam angle and the distance between the mirrors. A schematic diagram for the multi-pass cell with a typical spot pattern on the front mirror is shown in Figure 3-7. To prevent deposition of pump oil on the mirrors glass tubes are mounted around the mirrors. In addition, two resistive heaters are placed on the back of each mirror to keep their temperature about 40°C.

3.3 Electronic software

3.3.1 Data acquisition process

Acquiring data commences by sweeping the OPO light source across a frequency window of ~ 1.5 cm^{-1} by application of a sine wave to the PZT of the seed laser. The sine wave with 40 V amplitude and 100 Hz frequency is produced by the function generator (WaveTek 395) and amplified by the PZT driver. The function generator generates a Transistor-Transistor Logic (TTL) signal with the same frequency as the sine wave to synchronize the data acquisition setup. TTL signal activates counter 1 on the timer card which is responsible for synchronizing the other counters. Counter 2 initiates the data acquisition process in which the electronic signals from high-speed and low noise detectors are digitized. Recorded data is digitized at the rate of 10 MHz over the 1.6 ms time intervals.

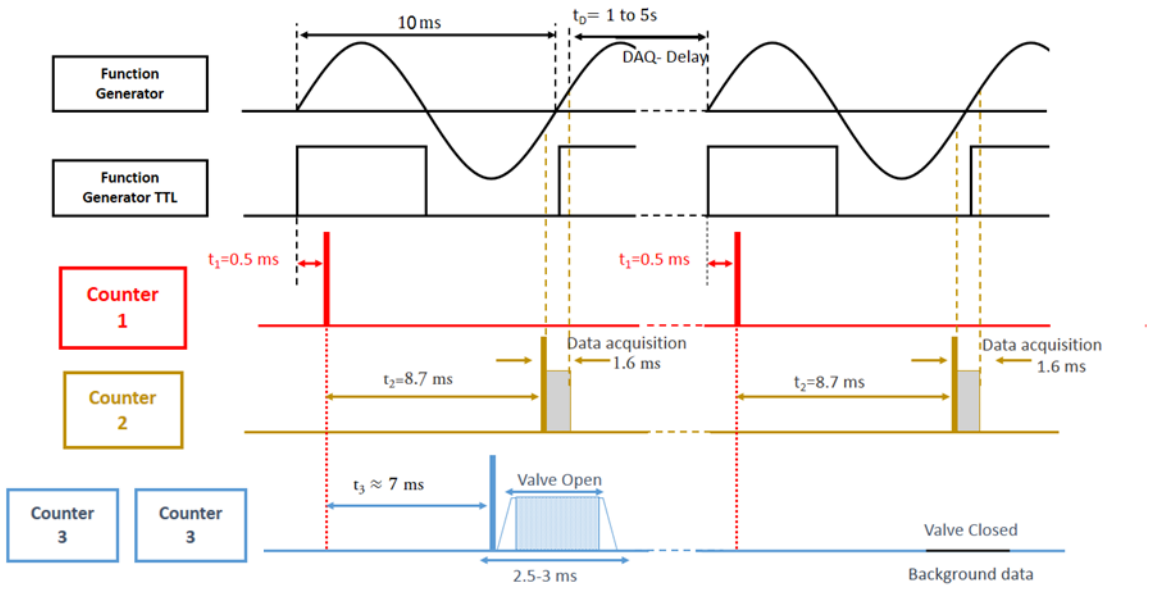

Figure 3-8: Timing sequence for data acquisition in OPO setup [49].

Data acquisition process takes place during the rising part of the sine wave and near the zero crossing where it has the steepest slope. Counters 3 and 4 are responsible for opening the valves.

Valves remain open for 3-4 ms to make sure that clusters are fully formed. After recording the data, diffusion pump removes the gas molecules from the six-way cross. This process takes 1-2 s. The above procedure is repeated with the valves closed. This scan is used to remove the background and generate a back ground free spectrum. Depending on the strength of the band of interest, this procedure is repeated for 100-500 times. The time sequence for data acquisition is shown in Figure 3-8. The procedure is managed by a LabVIEW program which will be explained in the next section.

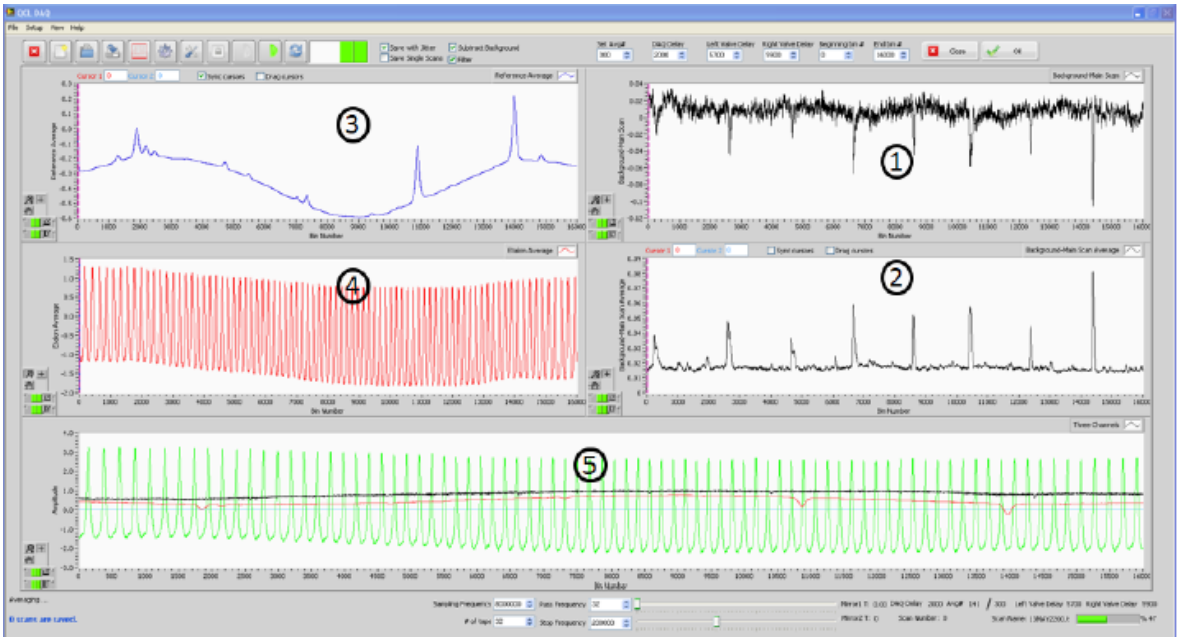

Figure 3-9: Screen-shot of the OPO control program. The numbered windows are: (1) main signal (jet channel); (2) average of the main signal; (3) average of the reference signal; (4) average of the etalon signal; (5) single scans of all three channels [49].

3.3.2 Control software

A LabVIEW program, is used to manage and control the data acquisition process and store the recorded data [49]. Counters, DAQ card, background subtraction and data storage are managed by

this program. Some of main features of this program are 1) jitter suppression, 2) digital filtering, and 3) power fluctuation suppression which will be explained briefly. Figure 3-9 shows a snapshot of the LabVIEW program developed for the OPO setup.

1) Jitter suppression: there are several sources of drift and jitter in frequency of the OPO light source such as mechanical vibrations, temperature instability, air pressure changes and laser current noise. Such frequency instabilities degrade the resolution of the recorded spectra and broaden the lines. In order to solve this problem a digital signal processing technique is used. In this technique, etalon peaks in the first scan are chosen as the reference. For each subsequent scan, the shift is calculated with respect to the reference. To match the frequency with the reference, the scans are shifted appropriately. Subsequently, laser jitters can be suppressed and data acquisition process is repeated to record the spectrum [49].

2) Digital filtering: there are some high frequency noises in the output of OPO light source which lower the SNR. In order to eliminate the high frequency noises, a finite impulse response (FIR) digital low-pass filter has been designed. Digital filter is used since it has many advantages such as arbitrary programing, no temperature dependency, no humidity drift and compatibility with the system [49].

3) Power fluctuation suppression: OPO power fluctuates and the fluctuations are repeated in all the scans in an unchanged pattern. As a result, these fluctuations cannot be removed by signal averaging technique. The effects of the power fluctuations would be significant in recording weak bands such as combination bands. A simple subtraction technique is implemented in the control software based on a balanced-detection method [56]. In this method, a refrence beam seperated from the probe light soruce is substracted electronically from the absorption signal. The reference

beam is called background signal. The background substracion method has led to significant improvements in recroding combination bands [49].

3.3.3 Post-data acquisition

Control software stores the data in a single-column text file. This file has recorded intensities for 16000 bin numbers. However, for data analysis and simulation we are interested in having line intensities versus wavenumbers (or frequencies). This conversion is achieved with the aid of Thermo Scientific GRAMS/AI^{TM} program as a platform. Known transitions from the reference gas are given as input. Then, the program makes the conversion by interpolation technique using the etalon peaks and reference frequencies. A snapshot of this program is shown in Figure 3-10. The top spectrum is the background free jet signal, the middle trace is the reference gas spectrum, and the bottom trace is the etalon spectrum. The signal at this level can be analyzed with PGOPHER software to obtain the rotational parameters for the ground and excited states.

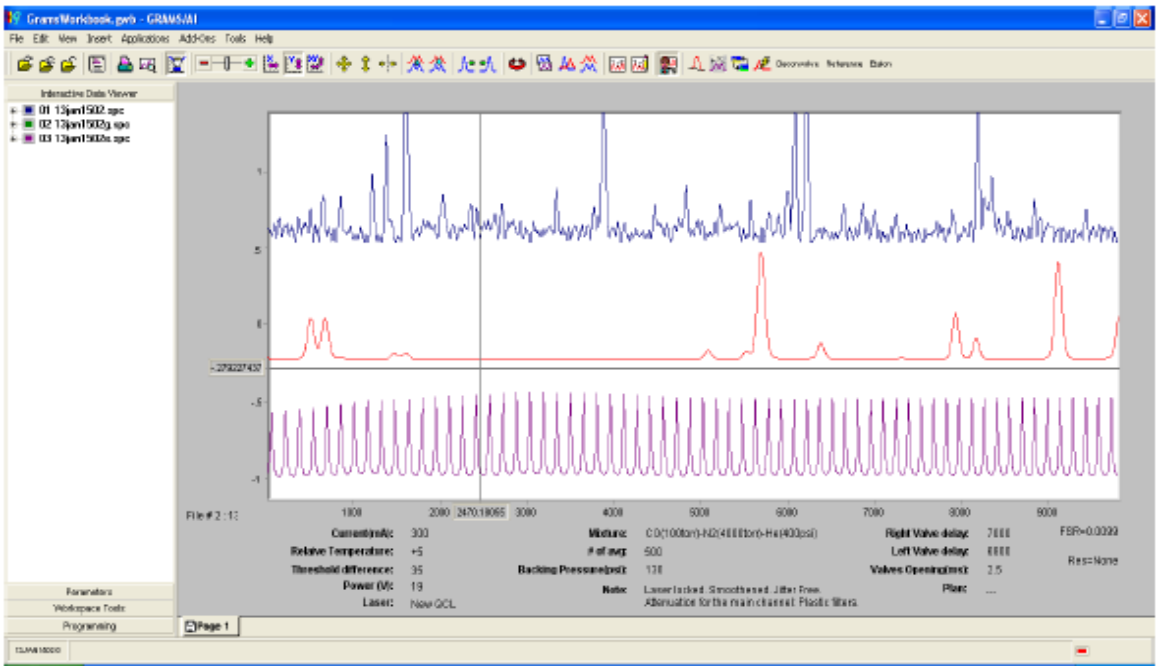

Figure 3-10: Snapshot of the GRAMS software.

Chapter Four: Results

Results of calculations using CAM-B3LYP functional performed on binary and ternary complexes of C_2D_2 and CS_2 are presented in this chapter. The optimized geometrical parameters of stationary structures and theoretical rotational constants are reported. These calculations indicate that the minimum energy structure of CS_2-C_2D_2 is a planar parallel configuration whereas the next higher energy isomer is T-shaped. They also show that a twisted-barrel configuration is the minimum energy isomer of the $(CS_2)_2$-C_2D_2 trimer. The two lowest energy isomers of CS_2-$(C_2D_2)_2$ trimer were also investigated. In this case, the global minimum structure has a distorted T-shaped C_2D_2 dimer unit with a CS_2 monomer "above" the dimer and the higher energy isomer was found to be planar. Finally, the observed rotationally-resolved infrared spectra of CS_2-C_2D_2 parallel dimer with C_{2v} symmetry and $(CS_2)_2$-C_2D_2 trimer with C_2 symmetry in the region of C_2D_2 ν_3 (~ 2439 cm^{-1}) fundamental are presented. Molecular parameters were found using the theoretical background presented in Chapter 2.

4.1 DFT calculations

4.1.1 C_2D_2-CS_2 dimer

DFT calculations using CAM-B3LYP functional were used to investigate binary complexes between CS_2 and C_2D_2 and to predict structures for the few lowest energy isomers. Configurations such as parallel, T-shaped, linear and cross-shaped were examined during the search for stationary structures. Geometry optimization on possible structures was also performed by changing the orientation of the monomers and varying the intermolecular distances to make sure that the

procedure converged to the same structure. The values obtained for the 15 (3N-6 harmonic oscillators) vibrational frequencies were examined to ensure that the obtained structure is indeed a minimum on the potential energy surface. For this to be the case, all of the vibrational frequencies must be real and positive.

Dimers of CS_2 with other members of the "CO_2 family" are known to form non-planar cross-shaped structures. For instance, CO_2-CS_2 dimer [56], a higher energy isomer of OCS-CS_2 [57] and CS_2 dimer [58] are all cross-shaped. We, therefore, thought that this might also be the case for CS_2-C_2H_2. But our search for a cross-shaped isomer was not successful.

Figure 4-1: Structure of CS_2-C_2D_2 dimer: a) the lowest energy isomer which is parallel; b) the higher energy isomer which is T-shaped.

The calculations resulted in two planar stationary configurations. The first isomer was found to be a parallel structure with C_{2v} symmetry. This parallel isomer can be described as two parallel monomers in which the line joining the centre of masses is perpendicular to the monomers axes. The second isomer, having a higher energy, was found to be a T-shaped configuration also with C_{2v} symmetry and CS_2 monomer forming the stem of the T. The structures for these isomers are shown in Figure 4-1. The other possible T-shaped structure with C_2D_2 monomer as stem of T was found to be a saddle point on the PES. Stationary geometries were fully optimized on bond lengths and angles using Gaussian 09 package. Ground state rotational constants were optimized at CAM-B3LYP level of theory with aug-cc-pVTZ basis set including empirical dispersion [59]. The

optimized rotational constants are listed in Table 4-1. Comparison of relative complexation energies (E) found from the DFT calculations using CAM-B3LYP hybrid functional and aug-cc-pVTZ basis set, shows that the parallel structure is the global minimum configuration on the PES.

Table 4-1: Calculated Rotational parameters of CS_2-C_2D_2 dimer.

	DFT	
	Parallel	T-shaped
E / cm^{-1}	-502	-388
A / MHz	2924.89	25219.98
B / MHz	1841.10	749.51
C / MHz	1129.88	727.88

Figure 4-2: Structure of $(CS_2)_2$-C_2D_2 trimer from two different views; side view (left) and top view (right).

4.1.2 $(CS_2)_2$-C_2D_2 trimer

Study of 3-body interactions was conducted by performing calculations on two possible mixed trimers formed from CS_2 and C_2D_2. In this case, MP2 method [60-62] with TZVP basis set [63, 64] was employed to find an initial guess and then DFT method at CAM-B3LYP level of theory with aug-cc-pVTZ basis set including empirical dispersion were used to optimize the structure. The calculations on the $(CS_2)_2$-C_2D_2 trimer resulted in a complex with C_2 symmetry where the C_2

axis is perpendicular to and passing through the center of mass of C_2D_2. "Top" and "side" views of this trimer are shown in Figure 4-2. The optimized rotational constants for the $(CS_2)_2$-C_2D_2 trimer are listed in Table 4-2.

Table 4-2: Calculated rotational parameters of $(CS_2)_2$-C_2D_2 trimer.

	DFT	MP2
A / MHz	1035.42	1071.79
B / MHz	553.09	610.78
C / MHz	545.32	574.32

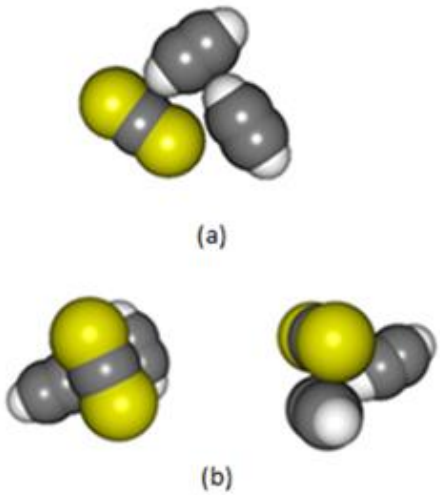

Figure 4-3: The two lowest energy isomers of CS_2-$(C_2D_2)_2$: (a) planar isomer as the higher energy isoemr; (b) the global minimum structure from two points of view; top view (left) and side view (right).

4.1.3 CS_2-$(C_2D_2)_2$ trimer

Using the same procedure, calculations for CS_2-$(C_2D_2)_2$ mixed trimer were made to explore the geometry of the lowest energy structure as well as structures of other low-lying energy isomers. The resulting two lowest energy isomers of the CS_2-$(C_2D_2)_2$ trimer are shown in Figure 4-3. Isomer

(a) is planar, Figure 4-3 (a), and can be described as a distorted T-shaped C_2D_2 dimer with a coplanar CS_2 beside the stem of the T. The second isomer, isomer (b) shown in Figure 4-3 (b), can be thought of as a distorted T-shaped C_2D_2 dimer unit with the CS_2 located "above" the plane of C_2D_2 dimer. The rotational constants for the ground state obtained from the calculations are reported in Table 4-3. Comparison of the relative complexation energies (E) shows that isomer (b) is the global minimum energy structure on the PES.

Table 4-3: Rotational constants for the two lowest energy isomers of the CS_2-(C_2D_2).

	DFT		MP2	
	Isomer 1	Isomer 2	Isomer 1	Isomer 2
E / cm^{-1}	-1385	-1481		
A / MHz	1534.75	1131.91	1516.75	1178.26
B / MHz	746.23	1025.56	742.40	1034.38
C / MHz	502.10	851.65	498.43	894.90

4.2 Experimental observations

4.2.1 Experimental details

The experimental observation of the predicted complexes was made by performing search scans near the C_2D_2 ν_3 (~2439 cm^{-1}) fundamental region. The desired complexes were generated in the supersonic slit-jet apparatus and probed using the OPO described in Chapter 3. The expansion gas was about 0.3% of CS_2 and 0.2% of C_2D_2 in helium. The backing pressure was 8 atm. Spectra were calibrated by using a fixed etalon (with a free spectral range of 0.00997 cm^{-1}) and a reference gas cell containing N_2O. Figure 4-4 shows a portion of the observed spectrum.

Ground state rotational constants obtained from the DFT calculations were used as a starting point for simulation of the recorded spectra. The PGOPHER program described in Chapter 2 was used for assignment, simulation, and fitting of the spectra. In the following sections, the analysis of the recorded bands will be described.

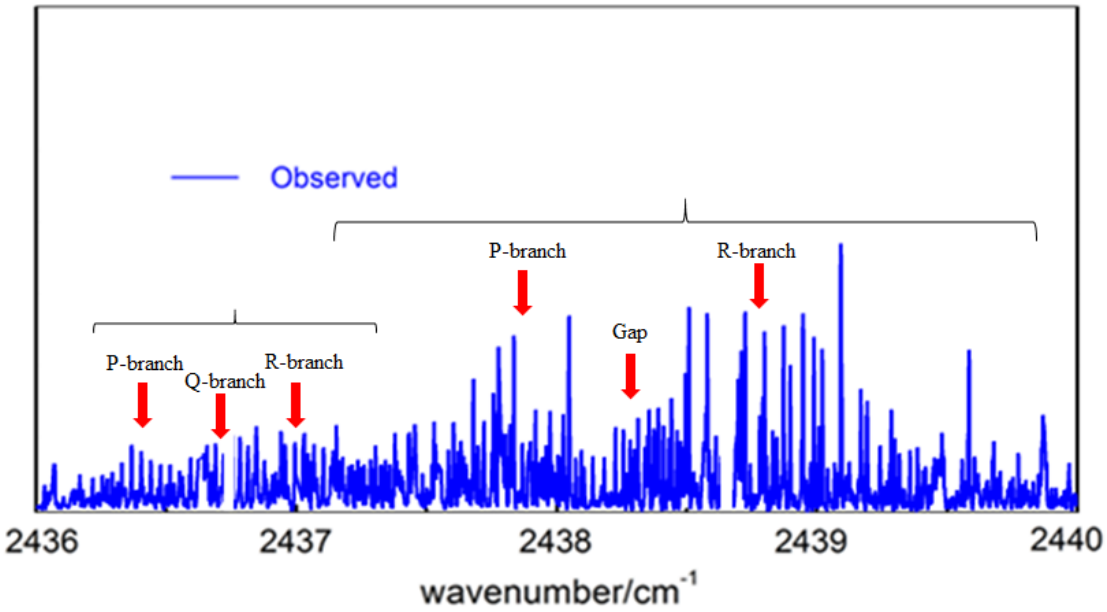

Figure 4-4: Observed ro-vibrational spectrum in C_2D_2 ν_3 region. Two new bands are presented. C_2D_2 monomer lines are removed from the spectrum.

4.2.2 Simulation of CS_2-C_2D_2 parallel dimer

The most stable isomer of CS_2-C_2D_2 with C_{2v} symmetry and its inertial axes are depicted in Figure 4-5. Here *a* and *b* are the inertial axes perpendicular and parallel to the monomers axes, respectively. We, therefore, expect one possible intramolecular fundamental in the region of the C_2D_2 ν_3 fundamental. This would be a *b*-type band with a characteristic intensity alternation in the spectrum due to nuclear spin statistics as listed in Table 4-4. Furthermore, as discussed in Chapter 2, a *b*-type band shows a gap around its band origin.

Using a mixture of C_2D_2 and CS_2, we observed two new bands to the lower side the of C_2D_2 monomer band origin as can be seen in Figure 4-4. The stronger of the two with a band center around 2438 cm^{-1} was assigned to CS_2-C_2D_2. This together with the trial simulation using the rotational parameters from the DFT calculations, see Table 4-1 , showed that the stronger of the two observed bands belongs to the parallel isomer. In the trial simulated spectrum, ground and excited states parameters were assumed to be equal.

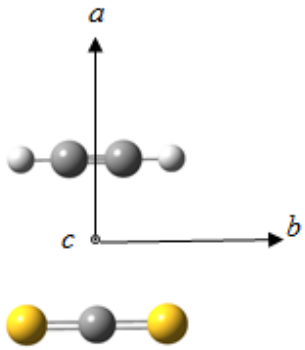

Figure 4-5: The principal axis system for CS_2-C_2D_2 parallel dimer.

Table 4-4: Nuclear spin weights of CS_2-C_2D_2 dimer for C_{2v} symmetry.

C_{2v}	A_1	A_2	B_1	B_2
	6	6	3	3

Subsequently, the PGOPHER program was used to perform detailed spectral analysis and to obtain experimental molecular parameters for the CS_2-C_2D_2 dimer. The rotational assignment was straightforward. We assigned a total of 89 transitions involving rotational levels up to $J = 12$. Seven ro-vibrational constants were fitted, 3 for the ground state and 4 for the excited vibrational state. The frequency analysis gave an excellent weighted standard deviation of 0.00036 cm^{-1}.

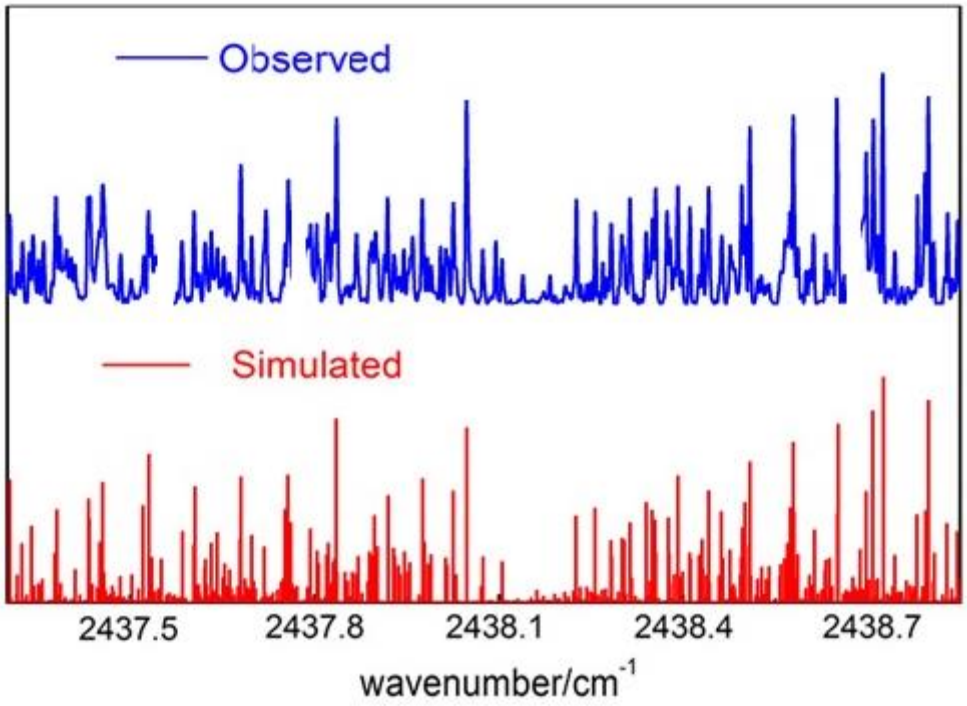

Figure 4-6: R-branch of the observed and simulated spectra of the planar C_2D_2-CS_2 dimer. The simulated spectrum used a rotational temperature of 3 K.. Blank regions in the observed spectrum are due to C_2D_2 monomer lines.

Table 4-5: Molecular parameters for parallel isomer of the CS_2-C_2D_2. Uncertainties in parentheses are 1σ from the least-squares fits in units of the last quoted digit.

	Excited state	Ground state
ν_0 / cm^{-1}	2438.165(1)	
A / MHz	2921.38(41)	2921.72(47)
B / MHz	1823.17(45)	1823.86 (44)
C / MHz	1120.11(39)	1119.93(38)
Δ / amu.Å^2		- 0.0071
$\Delta\nu_0$ / cm^{-1}		-1.079

Part of the observed and simulated spectra is shown in Figure 4-6. The rotational constants obtained from the fit are listed in Table 4-5. Higher order rotational constants, centrifugal distortion parameters, could not be determined. This is due to the fact that CS_2-C_2D_2 contains heavy atoms, resulting in rather small rotational constants. Thus, the low and intermediate *J* transitions observed in the experiments, described in this thesis, were not sufficient for the determination of the higher order terms. The planarity of CS_2-C_2D_2 was tested using

$$\frac{1}{C} = \frac{1}{A} + \frac{1}{B} \tag{4.1}$$

with the inertial defect defined as:

$$\Delta = I_c - I_a - I_b \tag{4.2}$$

For a planar molecule the inertial defect approaches zero. The measured inertial defect for CS_2-C_2D_2 is very small, -0.0071 $Å^2$, which indicates that the observed structure is indeed planar. Comparison of DFT results (Table 4-1) with experimental values (Table 4-5) shows that the ground state rotational constants are in very good agreement.

4.2.3 Observation of $(CS_2)_2$-C_2D_2 trimer

The lowest energy isomer of $(CS_2)_2$-C_2D_2 with C_2 symmetry and its inertial axes are shown in Figure 4-5. The principal axes for the trimer were found with the aid of PMIFST program [65] using the coordinates of the atoms from the DFT calculations. Here *c* is the inertial axes which is perpendicular to and passing through the center of mass of C_2D_2 monomer. Therefore, the only possible intramolecular fundamental in the region of the C_2D_2 ν_3 fundamental would be an *a*/*b*-type hybrid band. The nuclear spin statistics which results in a characteristic intensity alternation in the spectrum of $(CS_2)_2$-C_2D_2 are listed in Table 4-6. Consequently, levels with K_aK_c = ee and oe

(even even and odd even) in the ground vibrational state have a weight of 12, while levels with K_aK_c = eo and oo have weight of 6.

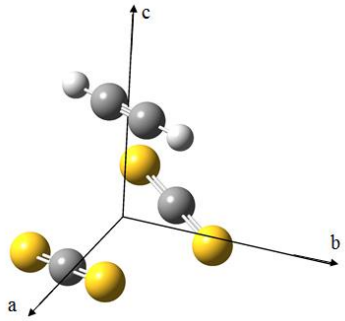

Figure 4-7: The principal axis system for $(CS_2)_2$-C_2D_2 trimer.

Table 4-6: Nuclear spin weights of $(CS_2)_2$-C_2D_2 timer for C_2 symmetry.

C_2	E	B
	12	6

The weaker of the two bands in the observed spectra with the band center of 2436.7 cm^{-1} was therefore assigned to the lowest energy isomer of $(CS_2)_2$-C_2D_2 trimer. To the higher side, this band overlaps with that of the CS_2-C_2D_2 dimer discussed in the previous section. There are also some interfering monomer lines near the band center which have been removed from the spectrum for clarity. Trial simulation of the band using the DFT rotational constants, listed in Table 4-2, confirmed that this band belongs to the lowest energy isomer of the $(CS_2)_2$-C_2D_2 trimer. As can be seen from comparison of the observed and simulated spectra, Figure 4-8, this band can be well simulated by *a*/*b*-type ro-vibrational transitions with a relative transition moment of *a*/*b*-type of about 0.7. A total of 83 transitions were assigned with values up to $J = 17$. The quality of the fit was very good, with a weighted rms deviation of 0.00034 cm^{-1}. Observed rotational constants form the fit are listed in Table 4-7.

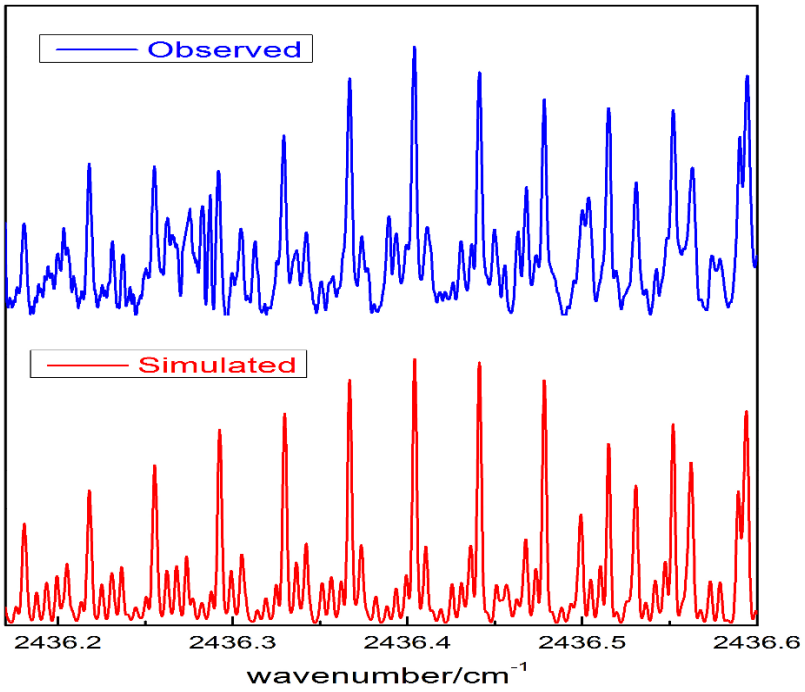

Figure 4-8: R-branch of the observed and simulated spectra of the $(CS_2)_2$-C_2D_2 trimer [1]. The simulated spectrum used a rotational temperature of 3 K.

Table 4-7: Molecular parameters for $(CS_2)_2$-C_2D_2 trimer. Uncertainties in parentheses are 1σ from the least-squares fits in units of the last quoted digit.

	Excited state	Ground state
ν_0 / cm^{-1}	2436.736(1)	
A / MHz	1025.7938(1)	1025.41(15)
B / MHz	552.87(22)	553.35 (19)
C / MHz	552.32(20)	552.76(20)
$\Delta\nu_0$ / cm^{-1}		-2.508

Chapter Five: Discussion and conclusions

Thanks to the availability of computational methods and high resolution spectroscopy, van der Waals complexes can be investigated in detail. Progress on the theoretical understanding of molecular structures has been very impressive. Theoretical investigations can serve as a guide for high resolution observations. On the other hand, detailed information obtained from high resolution spectroscopic data can be used for testing theoretical predictions and guiding the improvements of new computational methods. Recently, dimers, trimers and larger van der Waals complexes containing CO_2 family, CO_2, N_2O, CS_2 and OCS, with acetylene have been extensively studied. The interest in study of such species is due to the simplicity of the intermolecular forces among these species. Thus, it would be feasible to compare their theoretical and experimental structures.

In the present thesis, DFT calculations using CAM-B3LYP hybrid functional were used for the theoretical investigation of binary and ternary complexes formed from CS_2 and C_2D_2. We employed the calculations to predict structures for the few lowest energy isomers. DFT calculations predict that the two lowest energy isomers of CS_2-C_2D_2 dimer are planar. The global minimum has a parallel structure whereas the next higher energy isomer is T-shaped. In the case of $(CS_2)_2$-C_2D_2 the minimum energy isomer has a twisted-barrel configuration with C_2 symmetry. Furthermore, the most stable structure of CS_2-$(C_2D_2)_2$ trimer has a distorted T-shaped C_2D_2 dimer unit with the CS_2 monomer located “above” this dimer unit and the he higher energy isomer has a planar configuration.

The experimental results were obtained using high resolution infrared spectroscopy, described in Chapter 3. An OPO light source was used to probe the pulsed supersonic-jet expansion in the region of C_2D_2 ν_3 (~ 2439 cm^{-1}) fundamental band. We observed and analyzed two bands. One of these (centred at 2438.165 cm^{-1}) was assigned to the CS_2-C_2D_2 parallel dimer. Rotational constants and experimental geometry were found for the dimer. The observed *b*-type band assigned to this isomer has a red shift of 1.079 cm^{-1} with respect to the C_2D_2 ν_3 fundamental band. This red shift indicates that the overall strength of the intermolecular interaction is slightly stronger with excitation of the asymmetric stretching fundamental in C_2D_2. Moreover, the small measured inertial defect for the CS_2-C_2D_2 dimer, -0.0071 $Å^2$, shows that the observed parallel isomer is indeed planar.

A structure fitting program (STRFIT) [66] was used to find the experimental geometry of the CS_2-C_2D_2. Thanks to the high symmetry of the dimer, there is only one parameter needed to characterize its experimental structure. This parameter is the distance between the centres of mass of the two monomers. Here, we assume that the monomer's geometries remain unchanged upon complexation. The distance between the centers of mass was measured to be 3.6702(74) Å. The distance found from calculations was found to be (3.66 Å) which is in an excellent agreement with the experimental result. The structure of the lowest energy isomer of CS_2-C_2D_2 is analogous to the lowest energy isomer of CO_2-C_2H_2 [11-14]. In the case of CO_2-C_2H_2 the distance between the centres of mass of the two monomers was found to be 3.289 Å [11]. As expected, the measured distance for the CS_2-C_2D_2 dimer is greater than that for CO_2-C_2H_2 dimer due to the larger S atoms.

The band assigned to the $(CS_2)_2$-C_2D_2 trimer with C_2 symmetry (centred at 2436.736) was analyzed and rotational constants were measured. This band is 1.4 cm^{-1} to red side of the CS_2-C_2D_2 band. The observed vibrational red shift of 2.508 cm^{-1}, which is significantly larger than the

dimer's vibrational shift indicates that the overall strength of the intermolecular interaction on acetylene becomes stronger.

The growth of $(CS_2)_2$-C_2D_2 isomer can be explained as a CS_2 monomer being added "above" the CS_2-C_2D_2 parallel dimer. The added CS_2 monomer distorts the original parallel geometry of the CS_2-C_2D_2 dimer unit to form a trimer with C_2 symmetry. Although experimental rotational constants were obtained for $(CS_2)_2$-C_2D_2 trimer, these were not sufficient for complete structural determination. Assuming the monomers stay unchanged in the complex, five parameters, are required to completely define the structure. Three of which determine the structure of the CS_2 dimer subunit, and the remaining parameters specify the distance and orientation of the C_2D_2 monomer. See Figure 5.1 (a) and Table 5-1. Thus, there is a need for more experiments on different isotopologues of $(CS_2)_2$-C_2D_2 for complete experimental determination.

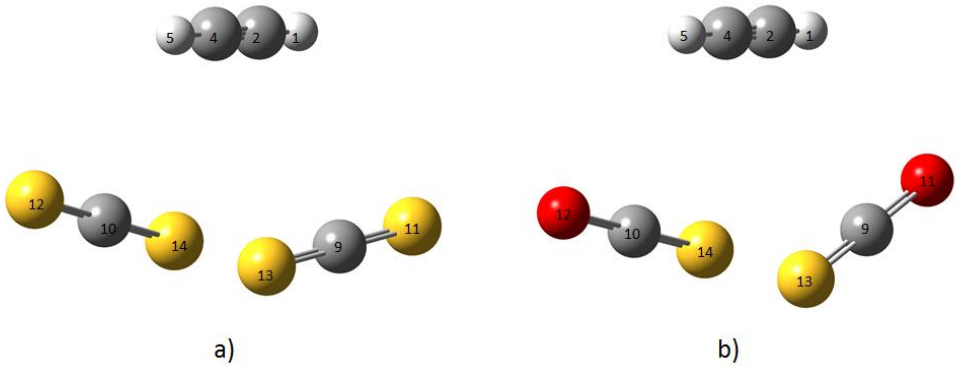

Figure 5.1: a) Theoretical structure of $(CS_2)_2$-C_2D_2 trimer; b) experimental structure of $(OCS)_2$-C_2H_2 lowest energy isomer. Atoms are numbered and the center of mass of acetylene is represented by M_3 whereas the center of CS_2 (OCS) dimer unit is represented by M_6. The centers of CS_2 (OCS) monomers are labeled as M_7 and M_8.

Because of the good agreement between the rotational constants of the complex obtained from the experimental spectra with those from calculations, it is reasonable to assume that the structural

parameters of $(CS_2)_2$-C_2D_2 are well represented by the DFT calculations. The calculated structural parameters for $(CS_2)_2$-C_2D_2 are listed in Table 5-1. Moreover, these parameters are compared with the experimental structure of the $(OCS)_2$-C_2H_2 trimer, see Figure 5.1 (b) [24]. As it can be seen in Table 5-1, the structural parameters of $(CS_2)_2$-C_2D_2 and $(OCS)_2$-C_2H_2 are fairly close. The structural information and observed rotational constants should enable assignment of future microwave spectra provided that the induced dipole moment in the complex is sufficient for the rotational spectra to be observed.

Table 5-1: Calculated structural parameters of $(CS_2)_2$-C_2D_2 trimer and experimental structural parameters of $(OCS)_2$-C_2H_2. θ shows the angle between three numbered atoms, while τ stands for dihedral angle.

Parameters	Calculated	Observed
	$(CS_2)_2$-C_2D_2	$(OCS)_2$-C_2H_2
r(M_6-M_3) /Å	3.07	3.121(2)
r(M_6-M_7) /Å	2.01	1.8238(6)
θ (M_{13}, M_7, M_8)/°	69.58	89.37(54)
τ (M_{13},M_7,M6,M3)/°	-77.47	-79.97(12)
τ (M7,M6,M3,M2)/°	78.84	87.5

In conclusion, the ground state rotational parameters obtained from DFT calculations (Table 4-1 and Table 4-2) are in very good agreement with their experimental counterparts (Table 4-5 and Table 4-7). The discrepancy in rotational constants is below 1%. In addition, the observation of the expected band types with their characteristic intensity alternation, ensures that the structures shown in Figure 4-5 and Figure 4-7 correspond to the complexes observed. Therefore, we have demonstrated that DFT calculations with a hybrid method and a large basis set can be used to guide the spectroscopic investigation of complexes formed from CS_2 and C_2D_2.

In our search for other complexes formed from CS_2 and C_2D_2, we have observed a band which might be due to the T-shaped isomer of dimer. However, there is a need for more measurements before the band can be assigned with certainty. We also have not been able to locate the bands for the other structures yet, but we hope to find them in CS_2 region. Intensity of vibration frequencies found from DFT calculations indicate that the intensity of the bands should be so stronger in the CS_2 asymmetric stretch region. Currently, we cannot cover this region with our probe lasers. A future study could be allocated to the observation of these structures in this region. Furthermore, In future, larger complexes can be studied by improving the resolution and SNR. Multi-pass absorption cell which was utilized in the present experiments was set nominally to 180 passes. This could be increased to 366 by careful adjustments of the orientation of the mirrors and the distance between the mirrors [67, 68]. As a result, the effective absorption path is increased and higher SNR would be achieved.

References

[1] A. Stone, *The Theory Of Intermolecular Forces*, Oxford University Press Inc, 2nd edition, (2013).

[2] D. D. Ebbing and S. D. Gammon, General Chemistry: Media Enhanced Edition, Cengage Learning, (2007).

[3] J. D. van der Waals, *On the Continuity of the Gaseous and Liquid States*, doctoral dissertation, Universiteit Leiden, (1873).

[4] I. Muller and W. H. Muller, *Fundamentals of Thermodynamics and Applications: With Historical Annotations and Many Citations from Avogadro to Zermelo*, Springer, (2009).

[5] V. Vedral and J. A. Dunningham, *Introductory Quantum Physics and Relativity*, Imperial College press, (2010).

[6] W.H. Marlow, J. Chem. Phys. **73**, 6288 (1980).

[7] C.M. Roth, B.L. Neal, and A.M. Lenhoff, Biophys. J. **70**, 977 (1996).

[8] R.R. Sauers, Bio. Med. Chem.y Lett. **5**, 2573 (1995).

[9] E. Hult and A. Kiejna, Surf. Scie. **383**, 88 (1997).

[10] N. Moazzen-Ahmadi and A.R.W. McKellar, Int. Rev. Phys. Chem. **32**, 611 (2013).

[11] D. G. Prichard, R. N. Nandi, J. S. Muenter, and B. J. Howard, J. Chem. Phys. **89**, 1245 (1988).

[12] Z. S. Huang and R. E. Miller, Chem. Phys. **132**, 185 (1989).

[13] J. S. Muenter, J. Chem. Phys. **90**, 4048 (1989).

[14] C. Lauzin, J. Norooz Oliaee, M. Rezaei, and N. Moazzen-Ahmadi, J. Mol. Spectrosc. **267**, 19 (2011).

[15] C. Lauzin, K. Didriche, T. Földes, and M. Herman, Mol. Phys. **109**, 2105 (2011).

[16] K. Didriche, T. Földes, C. Lauzin, and M. Herman, Mol. Phys. **110**, 2773 (2012).

[17] M. Rezaei, J. George, L. Welbanks, and N. Moazzen-Ahmadi, Mol. Phys. **112**, 2445 (2014).

[18] R. Bone and N. Handy, Theor. Chim. Acta. **78**, 133 (1990).

[19] W. de Almeida, Chem. Phys. **141**, 297 (1990).

[20] S. A. Peebles and R. L. Kuczkowski, J. Phys. Chem. **103**, 3884 (1999).

[21] S. A. Peebles and R. L. Kuczkowski, Chem. Phys. Lett. **312**, 357 (1999).

[22] J. Norooz Oliaee, M. Afshari, M. Dehghany, and N. Moazzen Ahmadi, A .R .W . McKellar, Chem. Phys. Lett. **257**, 133 (2009).

[23] S.A. Peebles and R.L. Kuczkowski, J. Chem. Phys. **111**, 10511 (1999).

[24] M. Rezaei, A.R.W. McKellar, and N. Moazzen-Ahmadi, J. Phys. Chem. A **115**, 10416 (2011).

[25] S.A. Peebles and R.L. Kuczkowski, J. Mol. Struct. (Theochem.) **500**, 391 (2000).

[26] H. Valdés and J.A. Sordo, Chem. Phys. Lett. **387**, 428 (2004).

[27] J. Norooz Oliaee, A.R.W. McKellar, and N. Moazzen-Ahmadi, Chem. Phys. Lett. **512**, 167 (2011).

[28] J.S. Muenter, J. Chem. Phys. **94**, 2781 (1991).

[29] H.-B. Qian, W. A. Herrebout, and B. J. Howard, Mol. Phys. **91**, 689 (1997).

[30] S. Sheybani-Deloui, M. Yousefi, J. Norooz Oliaee, A.R.W. McKellar, and N. Moazzen-Ahmadi, J. Mol. Spectrosc. **306**, 12 (2014).

[31] W.H. Press, S.A. Reukolsky, W.T. Vetterling, and B.P. Flannery, *Numerical Recipes in FORTRAN*, Second Edition, Cambridge University Press (1992).

[32] Philip R. Bunker and Per Jensen, *Molecular Symmetry and Spectroscopy, NRC Research Press*, Ottawa, 2nd edition (1998).

[33] P. Hohenberg and W. Kohn, Phys. Rev. **136**, 864 (1964).

[34] W. Kohn and L. J. Sham, Phys. Rev. **140**, 1133 (1965).

[35] R. G. Parr and Y. Weitao, *Density-Functional Theory of Atoms and Molecules*, Oxford University Press Inc (11940).

[36] A.D. Becke, J.Chem.Phys. **98**, 5648 (1993).

[37] C. Lee, W. Yang, R.G. Parr, Phys. Rev. B **37**, 785 (1988).

[38] S.H. Vosko, L. Wilk, M. Nusair, Can. J. Phys. **58**, 1200 (1980).

[39] P.J. Stephens, F.J. Devlin, C.F. Chabalowski, M.J. Frisch, J.Phys.Chem. **98**,11623 (1994).

[40] T. Yanai, D. Tew, and N. Handy, Chem. Phys. Lett. **393**, 51 (2004).

[41] Gaussian 09, M. J. Frisch, G. W. Trucks, H. B. Schlegel, G. E. Scuseria, M. A. Robb, J. R. Cheeseman, G. Scalmani, V. Barone, B. Mennucci, G. A. Petersson, H. Nakatsuji, M. Caricato, X. Li, H. P. Hratchian, A. F. Izmaylov, J. Bloino, G. Zheng, J. L. Sonnenberg, M. Hada, M. Ehara, K. Toyota, R. Fukuda, J. Hasegawa, M. Ishida, T. Nakajima, Y. Honda, O. Kitao, H. Nakai, T. Vreven, J. A. Montgomery, Jr., J. E. Peralta, F. Ogliaro, M. Bearpark, J. J. Heyd, E. Brothers, K. N. Kudin, V. N. Staroverov, R. Kobayashi, J. Normand, K. Raghavachari, A. Rendell, J. C. Burant, S. S. Iyengar, J. Tomasi, M. Cossi, N. Rega, J. M. Millam, M. Klene, J. E. Knox, J. B. Cross, V. Bakken, C. Adamo, J. Jaramillo, R. Gomperts, R. E. Stratmann, O. Yazyev, A. J. Austin, R. Cammi, C. Pomelli, J. W. Ochterski, R. L. Martin, K. Morokuma, V. G. Zakrzewski, G. A. Voth, P. Salvador, J. J. Dannenberg, S. Dapprich, A. D. Daniels, Ö. Farkas, J. B. Foresman, J. V. Ortiz, J. Cioslowski, and D. J. Fox, Gaussian, Inc., Wallingford CT, 2009.

[42] T. H. Dunning, J. Chem. Phys. **90**, 1007 (1989).

[43] D. E. Woon and T. H. Dunning, J. Chem. Phys. **98**, 1358 (1993).

[44] Philip R. Bunker and Per Jensen, *Molecular Symmetry and Spectroscopy*, NRC Research Press, Ottawa, 2nd edition (1998).

[45] D. Papouek and M. R. Aliev, *Molecular Vibrational-Rotational Spectra*, Elsevier Scientific Publishing Co., Amsterdam/Oxford/New York, (1982).

[46] C. M. Western, a program for simulating rotational structure PGOPHER, University of Bristol, UK; See http://pgopher.chm.bris.ac.uk.

[47] J. M. Hayes, Chem. Rev. **87**, 745 (1907)

[48] J. Koperski, Van der Waals Complexes in Supersonic Beams, Wiley-VCH, Weinheim, Germany (2003).

[49] M. Rezaei, *High-Resolution Pulsed Slit Jet Spectrometer with QCL and OPO probes for Infrared Spectroscopy on van der Waals Clusters*, PhD Thesis, University of Calgary (2014).

[50] W. Demtröder, *Laser Spectroscopy Basic Concepts and Instrumentation*, Springer (2003).

[51] C. M. Lovejoy and D. J. Nesbitt, Rev. Sci. Instrum. **58**, 807 (1987).

[52] R. H. Kingston, Proc. IRE **50**, 472 (1962).

[53] J. A. Giordmaine and R. C. Miller, Phys. Rev. Lett. **14**, 973 (1965).

[54] J. B. McManus, P. L. Kebabian, and M. S. Zahniser, App. Opt. **34**, 3336 (1995).

[55] W. Chen, G. Mouret, and D. Boucher, Appl. Phys. B **67**, 375 (1998).

[56] C. C. Dutton, D. A. Dows, R. Eikey, S. Evans, and R. A. Beaudet, J. Phys. Chem. A102, 6904 (1998).

[57] J. Norooz Oliaee, F. Mivehvar, M. Dehghany, and N. Moazzen-Ahmadi, J. Phys. Chem. A 114, 7311 (2010).

[58] M. Rezaei, J. Norooz Oliaee, N. Moazzen-Ahmadi, and A. R. W. McKellar, J. Chem. Phys. **134**, 144306 (2011).

[59] S. Grimme, S. Ehrlich, and L. Goerigk, J. Comp. Chem. 32, 1456 (2011).

[60] M. Head-Gordon, J. A. Pople, and M. J. Frisch, Chem. Phys. Lett. **153**, 503 (1988).

[61] M. J. Frisch, M. Head-Gordon, and J. A. Pople, Chem. Phys. Lett. **166**, 275 (1990).

[62] M. J. Frisch, M. Head-Gordon, and J. A. Pople, Chem. Phys. Lett. **166**, 281 (1990).

[63] A. Schaefer, H. Horn, and R. Ahlrichs, J. Chem. Phys. **97**, 2571 (1992).

[64] A. Schaefer, C. Huber, and R. Ahlrichs, J. Chem. Phys. **100**, 5829 (1994).

[65] Z. Kisiel, http://www.ifpan.edu.pl/ kisiel/struct/struct.htm.

[66] Z. Kisiel, J. Mol. Spectrosc **218**, 58 (2003).

[67] J. B. McManus, P. L. Kebabian, and M. S. Zahniser, Appl. Opt. 34 (18) 3336-3348 (1995).

[68] X. Liu, *High Resolution Mid-Infrared Spectroscopy of Molecular Complexes Containing Water and Ammonia*, PhD Thesis, University of Alberta (2013).

Appendix 1

Calculated and observed transitions for a parallel CS_2-D_2D_2 dimer:

J''	K_a''	K_c''	J'	k_a'	k_c'	Obs. (cm^{-1})	Cal. (cm^{-1})	Obs.-Cal.
1	1	0	1	0	1	2438.1050	2438.1052	-0.0002
2	1	1	2	0	2	2438.0736	2438.0735	0.0001
3	2	1	3	1	2	2438.0474	2438.0480	-0.0006
1	1	1	0	0	0	2438.0302	2438.0305	-0.0002
4	2	2	4	1	3	2438.0257	2438.0259	-0.0002
3	1	2	3	0	3	2438.0169	2438.0168	0.0001
2	0	2	1	1	1	2438.0138	2438.0137	0.0000
5	3	2	5	2	3	2437.9898	2437.9898	-0.0000
5	2	3	5	1	4	2437.9751	2437.9749	0.0002
3	2	2	3	1	3	2437.9451	2437.9453	-0.0001
7	4	3	7	3	4	2437.9291	2437.9283	0.0008
3	0	3	2	1	2	2437.9188	2437.9199	-0.0011
6	4	2	6	3	3	2437.9029	2437.9027	0.0002
4	2	3	4	1	4	2437.8929	2437.8926	0.0003
3	1	3	2	0	2	2437.8899	2437.8891	0.0008
5	1	4	5	0	5	2437.8540	2437.8539	0.0001
4	0	4	3	1	3	2437.8357	2437.8352	0.0005
5	2	4	5	1	5	2437.8300	2437.8297	0.0003
4	1	4	3	0	3	2437.8214	2437.8222	-0.0008
2	2	0	1	1	1	2437.8033	2437.8039	-0.0006
7	4	4	7	3	5	2437.7938	2437.7930	0.0008
5	0	5	4	1	4	2437.7573	2437.7563	0.0010
5	1	5	4	0	4	2437.7520	2437.7517	0.0003
4	2	3	3	1	2	2437.6975	2437.6979	-0.0004
6	0	6	5	1	5	2437.6800	2437.6801	-0.0001
5	2	4	4	1	3	2437.6419	2437.6419	0.0000
3	3	1	2	2	0	2437.6320	2437.6326	-0.0006
3	3	0	2	2	1	2437.6219	2437.6225	-0.0006
7	0	7	6	1	6	2437.6039	2437.6048	-0.0009
6	2	5	5	1	4	2437.5842	2437.5846	-0.0004
8	0	8	7	1	7	2437.5295	2437.5298	-0.0003
4	3	1	3	2	2	2437.5017	2437.5015	0.0001
5	3	3	4	2	2	2437.4843	2437.4838	0.0005
9	0	9	8	1	8	2437.4553	2437.4548	0.0005
8	2	6	7	3	5	2437.4102	2437.4103	-0.0002
10	0	1	9	1	9	2437.3790	2437.3796	-0.0006
7	3	5	6	2	4	2437.3856	2437.3864	-0.0008
5	4	1	4	3	2	2437.3247	2437.3245	0.0002
9	2	7	8	3	6	2437.3159	2437.3161	-0.0002
11	0	1	10	1	10	2437.3042	2437.3042	-0.0000
6	4	3	5	3	2	2437.2607	2437.2607	-0.0000
12	0	1	11	1	11	2437.2289	2437.2285	0.0004
6	4	2	5	3	3	2437.2046	2437.2044	0.0003

7	4	4	6	3	3	2437.2008	2437.2005	0.0003
7	6	2	6	5	1	2436.9410	2436.9418	-0.0007
7	6	1	6	5	2	2436.9410	2436.9409	0.0001
1	0	1	1	1	0	2438.2261	2438.2254	0.0007
2	0	2	2	1	1	2438.2567	2438.2570	-0.0002
3	1	2	3	2	1	2438.2826	2438.2822	0.0004
0	0	0	1	1	1	2438.2997	2438.3001	-0.0004
4	1	3	4	2	2	2438.3033	2438.3039	-0.0005
3	0	3	3	1	2	2438.3130	2438.3135	-0.0005
5	2	3	5	3	2	2438.3394	2438.3393	0.0001
6	2	4	6	3	3	2438.3497	2438.3492	0.0005
4	2	2	4	3	1	2438.3549	2438.3536	0.0013
3	1	3	3	2	2	2438.3856	2438.3852	0.0004
7	2	5	7	3	4	2438.3909	2438.3912	-0.0003
7	3	4	7	4	3	2438.3978	2438.3988	-0.0010
2	1	2	3	0	3	2438.4107	2438.4106	0.0001
6	3	3	6	4	2	2438.4255	2438.4256	-0.0002
4	2	3	4	3	2	2438.4308	2438.4300	0.0008
2	0	2	3	1	3	2438.4413	2438.4415	-0.0002
5	2	4	5	3	3	2438.4624	2438.4618	0.0006
5	0	5	5	1	4	2438.4764	2438.4759	0.0004
3	1	3	4	0	4	2438.4949	2438.4953	-0.0003
3	2	2	4	1	3	2438.5004	2438.5009	-0.0005
3	0	3	4	1	4	2438.5084	2438.5082	0.0001
7	1	6	7	2	5	2438.5211	2438.5205	0.0006
1	1	1	2	2	0	2438.5266	2438.5266	0.0000
7	3	5	7	4	4	2438.5344	2438.5346	-0.0003
7	4	3	7	5	2	2438.5394	2438.5392	0.0003
4	1	4	5	0	5	2438.5733	2438.5740	-0.0007
4	0	4	5	1	5	2438.5789	2438.5786	0.0003
4	2	3	5	1	4	2438.6117	2438.6122	-0.0005
7	0	7	7	1	6	2438.6380	2438.6381	-0.0001
2	2	0	3	3	1	2438.6975	2438.6978	-0.0002
2	2	1	3	3	0	2438.7093	2438.7079	0.0014
6	0	6	7	1	7	2438.7243	2438.7251	-0.0008
5	1	4	6	2	5	2438.7441	2438.7447	-0.0006
3	2	1	4	3	2	2438.7811	2438.7801	0.0010
6	1	5	7	2	6	2438.8073	2438.8081	-0.0008
4	2	2	5	3	3	2438.8463	2438.8458	0.0005
8	0	8	9	1	9	2438.8723	2438.8726	-0.0003
5	2	3	6	3	4	2438.8980	2438.8976	0.0005
5	4	2	6	5	1	2439.1936	2439.1942	-0.0006
5	4	1	6	5	2	2439.1909	2439.1903	0.0006
5	5	0	6	6	1	2439.2864	2439.2866	-0.0002
5	5	1	6	6	0	2439.2864	2439.2867	-0.0003
7	4	3	8	5	4	2439.3578	2439.3580	-0.0002
6	5	1	7	6	2	2439.3864	2439.3863	0.0000
6	5	2	7	6	1	2439.3864	2439.3871	-0.0008
7	6	2	8	7	1	2439.5815	2439.5809	0.0006

7	6	1	8	7	2	2439.5815	2439.5808	0.0007
8	6	3	9	7	2	2439.6795	2439.6805	-0.0009
9	0	9	10	1	10	2438.9469	2438.9460	0.0009
4	4	0	5	5	1	2439.0920	2439.0920	-0.0000
4	4	1	5	5	0	2439.0920	2439.0924	-0.0004
9	6	3	10	7	4	2439.7746	2439.7751	-0.0005
6	6	1	7	7	0	2439.4807	2439.4809	-0.0002
6	6	0	7	7	1	2439.4807	2439.4809	-0.0002
7	4	4	8	5	3	2439.4173	2439.4168	0.0005
8	5	4	9	6	3	2439.5912	2439.5922	-0.0010
8	2	6	9	3	7	2439.0416	2439.0411	0.0005
5	3	2	6	4	3	2439.0681	2439.0682	-0.0001
4	2	3	5	3	2	2438.9765	2438.9766	-0.0002
7	3	5	8	2	6	2438.9169	2438.9167	0.0002
9	6	4	10	7	3	2439.7795	2439.7801	-0.0007
7	7	1	8	8	0	2439.6749	2439.6749	0.0000
7	7	0	8	8	1	2439.6749	2439.6749	0.0000

Appendix 2

Calculated and observed transitions for a twisted barallel $(CS_2)_2$-D_2D_2 trimer:

J''	K_a''	K_c''	J'	k_a'	k_c'	Obs. (cm^{-1})	Cal. (cm^{-1})	Obs.-Cal.
5	5	0	5	5	1	2436.7362	2436.7367	-0.0006
6	6	0	6	6	1	2436.7362	2436.7367	-0.0005
4	4	0	4	4	1	2436.7362	2436.7368	-0.0006
5	1	4	4	1	3	2436.5517	2436.5520	-0.0003
6	0	6	5	0	5	2436.5147	2436.5150	-0.0003
7	1	6	6	1	5	2436.4781	2436.4779	0.0002
8	0	8	7	0	7	2436.4410	2436.4408	0.0002
9	1	8	8	1	7	2436.4038	2436.4036	0.0002
0	0	10	9	0	9	2436.3669	2436.3665	0.0004
11	2	10	10	2	9	2436.3293	2436.3293	-0.0000
12	0	12	11	0	11	2436.2922	2436.2921	0.0001
13	1	12	12	1	11	2436.2546	2436.2546	-0.0000
14	0	14	13	0	13	2436.2174	2436.2175	-0.0001
15	1	14	14	1	13	2436.1799	2436.1800	-0.0000
16	0	16	15	0	15	2436.1428	2436.1428	0.0000
17	1	16	16	1	15	2436.1053	2436.1052	0.0002
4	0	4	5	0	5	2436.9210	2436.9209	0.0001
6	0	6	7	0	7	2436.9946	2436.9943	0.0003
8	0	8	9	0	9	2437.0679	2437.0675	0.0004
9	2	8	10	2	9	2437.1044	2437.1042	0.0003
10	1	10	11	1	11	2437.1409	2437.1406	0.0003
8	3	6	9	4	5	2437.1777	2437.1780	-0.0003
9	3	6	10	4	7	2437.2141	2437.2146	-0.0006
7	2	6	7	3	5	2436.8142	2436.8149	-0.0007
11	10	2	1	10	9	2436.0318	2436.0311	0.0008
12	10	2	11	9	3	2435.9936	2435.9938	-0.0002
13	10	4	12	9	3	2435.9562	2435.9566	-0.0003
8	5	4	8	4	5	2436.5936	2436.5942	-0.0005
9	5	4	9	4	5	2436.5936	2436.5939	-0.0002
3	2	2	2	1	1	2436.5787	2436.5788	-0.0002
4	1	4	3	0	3	2436.5740	2436.5734	0.0006
7	1	7	6	0	6	2436.4627	2436.4624	0.0003
4	3	2	5	4	1	2437.0306	2437.0314	-0.0008
3	1	2	4	1	3	2436.8839	2436.8842	-0.0002
9	5	4	9	6	3	2436.9091	2436.9093	-0.0002
10	5	6	1	10	6	2436.9091	2436.9090	0.0001
7	3	4	7	2	5	2436.6568	2436.6573	-0.0004
9	6	4	9	5	5	2436.5624	2436.5625	-0.0001
10	6	4	1	10	5	2436.5624	2436.5622	0.0003
6	0	6	5	1	5	2436.5304	2436.5306	-0.0003
6	2	4	5	1	5	2436.4676	2436.4676	-0.0000
5	5	0	6	6	1	2437.1316	2437.1314	0.0002
5	4	2	6	5	1	2437.1002	2437.0997	0.0004

6	5	2	7	6	1	2437.1684	2437.1681	0.0003
6	1	6	6	2	5	2436.7835	2436.7837	-0.0002
6	0	6	6	1	5	2436.7524	2436.7522	0.0002
7	1	6	7	0	7	2436.7199	2436.7199	-0.0000
6	2	4	6	1	5	2436.6892	2436.6891	0.0001
4	0	4	3	0	3	2436.5897	2436.5891	0.0006
4	0	4	3	1	3	2436.6044	2436.6048	-0.0004
4	2	2	3	1	3	2436.5421	2436.5418	0.0003
7	2	6	6	1	5	2436.4304	2436.4309	-0.0004
5	5	0	4	4	1	2436.4114	2436.4105	0.0009
8	2	6	7	1	7	2436.3934	2436.3933	0.0001
6	6	0	5	5	1	2436.3423	2436.3420	0.0002
7	5	2	6	4	3	2436.3362	2436.3363	-0.0001
8	7	2	7	6	1	2436.2368	2436.2365	0.0003
9	6	4	8	5	3	2436.2303	2436.2307	-0.0004
0	10	5	1	9	4	2436.2252	2436.2249	0.0002
8	8	0	7	7	1	2436.2051	2436.2052	-0.0000
9	7	2	8	6	3	2436.1989	2436.1993	-0.0005
10	6	4	9	5	5	2436.1932	2436.1935	-0.0003
11	5	6	10	4	7	2436.1881	2436.1877	0.0004
10	7	4	9	6	3	2436.1622	2436.1622	-0.0000
9	9	0	8	8	1	2436.1367	2436.1367	0.0000
10	8	2	9	7	3	2436.1308	2436.1308	-0.0001
11	7	4	10	6	5	2436.1249	2436.1250	-0.0001
10	9	2	9	8	1	2436.1000	2436.0995	0.0005
12	7	6	11	6	5	2436.0875	2436.0877	-0.0002
11	8	4	10	7	3	2436.0930	2436.0936	-0.0007
10	10	0	9	9	1	2436.0682	2436.0683	-0.0000
11	9	2	10	8	3	2436.0624	2436.0623	0.0001
12	8	4	11	7	5	2436.0561	2436.0564	-0.0003
11	11	0	10	10	1	2436.0001	2435.9998	0.0003
4	4	0	5	5	1	2437.0637	2437.0630	0.0007
8	2	6	9	3	7	2437.1464	2437.1464	-0.0000
7	4	4	8	5	3	2437.1730	2437.1731	-0.0001
9	2	8	10	3	7	2437.1826	2437.1830	-0.0004
8	4	4	9	5	5	2437.2099	2437.2097	0.0002
7	7	0	8	8	1	2437.2681	2437.2681	-0.0000
8	6	2	9	7	3	2437.2732	2437.2730	0.0002
9	5	4	10	6	5	2437.2782	2437.2779	0.0002
9	8	2	10	9	1	2437.3731	2437.3731	-0.0000